Japanese Journal of Applied Physics

Diffractive Optic Synthesis and Analysis of Light Fields and Recent Applications

To cite this article: Hwi Kim *et al* 2006 *Jpn. J. Appl. Phys.* **45** 6555

Japanese Journal of Applied Physics
Vol. 45, No. 8B, 2006, pp. 6555–6575

Review Paper

Diffractive Optic Synthesis and Analysis of Light Fields and Recent Applications

Hwi KIM, Kyongsik CHOI and Byoungho LEE*

School of Electrical Engineering, Seoul National University, Kwanak-Gu Shinlim-Dong, Seoul 151-744, Korea

(Received March 6, 2006; accepted April 5, 2006; published online August 22, 2006)

The synthesis and analysis of light fields having specific properties are the main issues in diffractive optics. Light field synthesis technology with diffractive optical elements can provide actual solutions for various applications that require extraordinary optical functions. Also, the rigorous analysis of a light field is an essential element for the design and application of micro- or nanoscale diffractive optical elements. In this paper we review the theoretical aspects of the diffractive optic synthesis and analysis of light fields, and present some recent applications of diffractive optical elements for information, nano-, and biotechnologies. [DOI: 10.1143/JJAP.45.6555]

KEYWORDS: light field synthesis, diffractive optical element, diffraction analysis

1. Introduction

It is interesting to note that although Rayleigh pointed out the theoretical possibility of a surface relief structure of diffractive optical elements (DOEs), he commented that "It is not likely that such a result will ever be fully attained in practice" due to the requirement of subwavelength height accuracy.[1,2] At present, we can implement surface relief diffractive optical devices by means of modern technologies such as lithography or diamond turning. We now are also equipped with holography technologies to make holographic optical elements (HOEs) as well. Another important technology is the development of dynamic modulators such as liquid crystal devices or micro-electro-mechanical systems that enable dynamic diffractive optical devices.

Diffractive optics has been greatly advanced particularly during the last two decades with the rapid progress of fabrication and computer technologies.[3–6] Light field synthesis techniques with DOEs provide actual solutions for various applications that require extraordinary optical functions such as laser beam shaping, display, optical interconnection and switching, manipulating nanoparticles, and bio-sensors.

It can be said that the primary function of DOEs is the synthesis of any desired light field distribution in a specified space domain. The specified space domain can be a two-dimensional (2D) flat surface, a 2D curved surface or a three-dimensional (3D) volume. In most cases, the goal of designing a DOE is to form the required optical intensity distributions on a 2D surface[3–18] or in a 3D volume.[19–26] The synthesis of light fields that satisfy the required properties in a 2D space domain is now well understood.[3–18] During recent years, the 2D domain problem was generalized to the 3D domain problem and the feasibility of 3D field synthesis was demonstrated. The 3D field synthesis problem requires some advanced understanding and generalization of constraints and limitations related to the properties of 3D fields.[20,22)]

Diffractive optic field analysis is also an important area of research, particularly because of the recent interest in micro- or nanoscale diffractive structures such as subwavelength DOEs, surface plasmon devices, and photonic crystals. Of course, the primary purpose of using those effects or devices is also to synthesize any desired light field. However, the design of these devices requires very different approaches and we must have good tools for analyzing diffractive optics in these cases.

In this paper, we discuss the light field synthesis problem using DOE, particularly with respect to its theoretical aspects. The synthesis problems can be classified by the dimensionality, 2D or 3D, and each problem can also be subdivided according to specifications and optimization techniques. The 2D/3D synthesis problems and optimization techniques can be described with a unified formalism. The diffractive field analyses for subwavelength DOEs and surface plasmon resonance are also briefly explained. We discuss some recent applications of DOEs to information, nano-, and biotechnologies.

The diffractive optic synthesis and analysis of light is an important field of research and has been intensively researched. Hence, it is not possible to review all relevant sub-topics in these areas in this limited-length paper. The purpose of this review paper is not to review diffractive optics completely but to provide an overview on some current interests in these fields.

This paper is organized as follows. In §2, as a prerequisite to the main contents, the methods of representing light fields are reviewed and the light field propagation through a general DOE optical system is explained with these representations. In §3, a mathematical modeling of the light field synthesis problem is accounted for. The light field synthesis problems and the strategies for solving them are presented. In §4, diffractive optic analysis methods of light fields are discussed. In §5, some applications of DOEs are presented and finally, concluding remarks follow in §6.

2. Light Field Propagation through General DOE Optical System

From diffraction theory, it is well understood that the whole spatial field distribution in the free space can be governed by the surface boundary condition.[27,28] Thus, the basic strategy for synthesizing a light field in the output domain is to find an appropriate surface field distribution on the specified input plane (DOE domain) and manipulate the obtained surface boundary condition using a light field modulator, as shown in Fig. 1. The surface boundary condition can be realized with light field modulators such as surface relief DOEs, HOEs, computer-generated holography (CGH) films or dynamic DOEs adopting phase-type spatial light modulators (SLMs). In this paper, we focus on

*Corresponding author. E-mail address: byoungho@snu.ac.kr

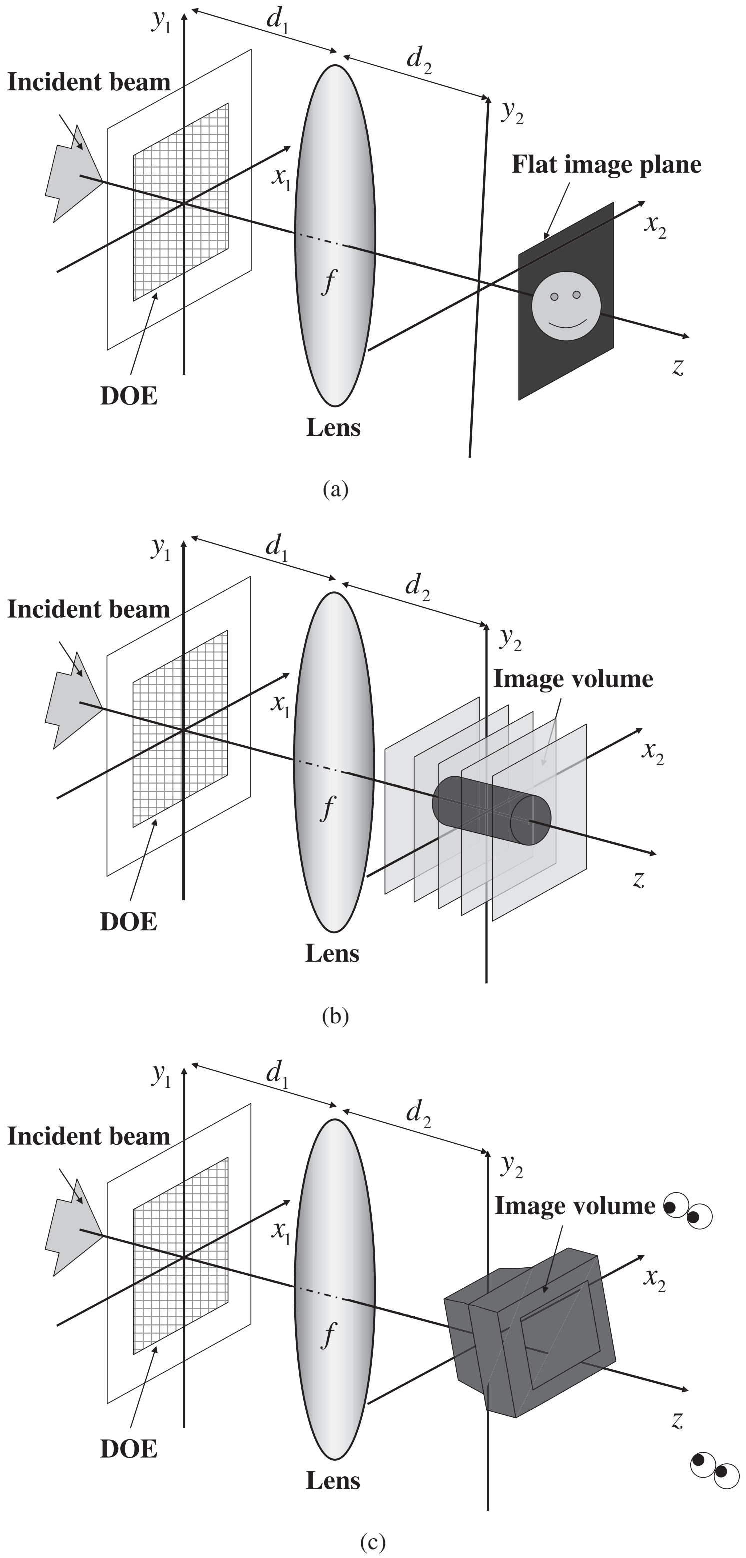

Fig. 1. (a) 2D domain intensity distribution synthesis problem, (b) 3D domain intensity distribution synthesis problem, (c) 3D image synthesis problem.

DOEs. In most cases, phase-only devices that modulate only the phase profiles of the incident optical wave (while maintaining the pregiven amplitude profile) are attractive due to their high transmission efficiency and/or simple fabrication. Although absorption-type DOEs also exist, we only focus on the design of phase-only elements in this paper. Another issue of much study is the effect of low coherent light in DOEs.[29,30] However, this issue will not be considered in this paper. Hence, we assume coherent light in our discussion on diffractive optic synthesis.

In the paraxial approximation regime, all wavefront modulators such as lenses and DOEs are modeled by the thin element approximation (TEA). The light modulated by a TEA device is also a paraxial light field. Although the more refined transmittance model of DOE and the non-paraxial regime vectorial field phenomena are not included in this limited-length paper, there are many publications on those topics.[31–37] The paraxial light field in free space can be described with various representation schemes. The most popular schemes are the Fourier representation (angular spectrum representation) and the Hermite-Gaussain-mode representation. Nowadays, fractional Fourier transform[38] is being looked upon as a powerful analysis tool for the paraxial field, but in this paper, we do not deal with the fractional Fourier transform. In this section, we review the Fourier and Hermite-Gaussian representations of paraxial light fields and present the field propagation through a general optical system with a DOE using the Fourier representation and the Hermite-Gaussian representation.

2.1 Field representation

The paraxial Fresnel diffraction integral is obtained from the first kind Rayleigh–Sommerfeld diffraction integral with the paraxial approximation (the Fresnel approximation). This is introduced in many text books (see, for example, refs. 27 and 28). The Fresnel diffraction integral can also be directly derived from the Fourier representation (angular spectrum representation). The Fourier representation of the diffraction field $F(x,y,z)$ is given by

$$F(x,y,z) = \iint_{-\infty}^{\infty} A(\alpha,\beta)\exp\left[j2\pi\left(\alpha x + \beta y + \sqrt{(1/\lambda)^2 - \alpha^2 - \beta^2 z}\right)\right] d\alpha\, d\beta, \tag{1}$$

where $A(\alpha,\beta)$ denotes the angular spectrum of the light field on the DOE plane (see Fig. 1), $\alpha = k_x/2\pi$, $\beta = k_y/2\pi$ ($\mathbf{k}$ is the wave vector), and λ is the wavelength of light. In the paraxial regime, the light field is then obtained as

$$F(x,y,z) = \exp[j2\pi z/\lambda] \iint_{-\infty}^{\infty} A(\alpha,\beta)\exp[j2\pi(\alpha x + \beta y)]\exp[-\pi\lambda z(\alpha^2 + \beta^2)]\, d\alpha\, d\beta. \tag{2}$$

The Fourier coefficient $A(\alpha,\beta)$ is represented by the field $F(x,y,0)$ at the input plane ($z = 0$) as

$$A(\alpha,\beta) = \iint_{-\infty}^{\infty} F(x',y',0)\exp[-j2\pi(\alpha x' + \beta y')]\, dx'\, dy' \tag{3}$$

By substituting eq. (3) into eq. (2), the diffraction field $F(x,y,z)$ reads as

$$\begin{aligned} &F(x,y,z) \\ &= \exp[j2\pi z/\lambda] \iint_{-\infty}^{\infty} F(x',y',0)\left\{\iint_{-\infty}^{\infty} \exp[-j\pi\lambda z(\alpha^2+\beta^2)]\exp[j2\pi(\alpha(x-x') + \beta(y-y'))]\, d\alpha\, d\beta\right\} dx'\, dy' \\ &= \frac{\exp[j2\pi z/\lambda]}{j\lambda z} \iint_{-\infty}^{\infty} F(x',y',0)\exp\left[\frac{j\pi}{\lambda z}((x-x')^2 + (y-y')^2)\right] dx'\, dy' \end{aligned} \tag{4}$$

The final expression of eq. (4) is known as the Fresnel diffraction integral (Fresnel transform).

The Hermite-Gaussian modes (Hermite-Gaussian beams) are a complete orthonomal set of solutions of the paraxial wave equation.[38] Let the nth-order Hermite-Gaussian mode be denoted by $\psi_n(x)$. An important mathematical property of the Hermite-Gaussian modes is that the Hermite-Gaussian mode expands the Fresnel transform kernel as

$$\sum_{n=0}^{\infty} e^{-jn\alpha}\psi_n(u)\psi_n(u') = \sqrt{1 - j\cot\alpha}\,\exp[j\pi(u^2\cot\alpha - 2uu'\csc\alpha + u'^2\cot\alpha)], \tag{5}$$

where the right side is a mathematically equivalent form of the kernel of the Fresnel diffraction integral of eq. (4). Let $\alpha = \arctan(z/\breve{z})$, $u' = x'/W_0$ $u = x/W(z)$, $W_0^2 = \lambda\breve{z}$ and $1/(z - j\breve{z}) = 1/R(z) + j\lambda/W^2(z)$, where $W(z)$ and $R(z)$ denote the beam size and the wavefront radius of curvature, respectively. Substituting these equations into eq. (5), with the aid of the orthonormal property of the Hermite-Gaussian modes, we can easily obtain

$$\begin{aligned} &\frac{\exp[jkz]}{W(z)}\psi_g\left(\frac{x}{W(z)}\right)\psi_h\left(\frac{y}{W(z)}\right)\exp\left[jk\frac{x^2+y^2}{2R(z)} - j(g+h+1)\varsigma(z)\right] \\ &\quad = \frac{\exp[jkz]}{j\lambda z}\iint \frac{1}{W_0}\psi_g\left(\frac{x'}{W_0}\right)\psi_h\left(\frac{y'}{W_0}\right)\exp\left[\frac{jk}{2z}((x-x')^2 + (y-y')^2)\right] dx'\, dy', \end{aligned} \tag{6a}$$

where $\varsigma(z)$ is the Gouy phase shift defined by

$$\varsigma(z) = \arctan\left(\frac{\lambda z}{W_0^2}\right). \tag{6b}$$

An arbitrary field on the input plane ($z = 0$), $F(x',y',0)$, can be expanded by the Hermite-Gaussian modes as

$$F(x',y',0) = \sum_{g,h} C_{gh}\frac{1}{W_0}\psi_g\left(\frac{x'}{W_0}\right)\psi_h\left(\frac{y'}{W_0}\right), \tag{7}$$

where W_0 means the common width of the Hermite-Gaussian modes and C_{gh} is the complex coefficient (called the Hermite-Gaussian transform coefficient). Then the diffraction field $F(x, y, z)$ is given, using eq. (6a), as

$$F(x,y,z) = \sum_{g,h} C_{gh} \frac{\exp[jkz]}{W(z)} \psi_g\left(\frac{x}{W(z)}\right)\psi_h\left(\frac{y}{W(z)}\right) \exp\left[jk\frac{x^2+y^2}{2R(z)} - j(g+h+1)\varsigma(z)\right]. \tag{8}$$

Then $\varsigma(z)$ indicates the Guoy phase.

2.2 Light field propagation

The mathematical model of the general optical system with a DOE is established in this subsection. Figure 1(a) shows the schematic of the paraxial optical system with a DOE. A phase-only DOE placed in the input plane and a thin lens of focal length f constitute the optical system. Let the distance from the DOE plane to the lens and that from the lens to the image plane be d_1 and d_2, respectively. An incident coherent optical wave with wavelength of λ impinges on the back of the DOE and passes through the DOE with its phase modified. The modulated surface boundary field distribution generates a diffracted field distribution in the output image plane or volume.

The optical wave propagation through the general optical system with a DOE can be described with the Fourier or the Hermite-Gaussian mode representation. There are several mathematical models of the optical system.[38] A popular one is the linear canonical transform (LCT) called the generalized Fresnel transform.[14,38] Also, the characteristics of the optical system can be described in the phase space.[38–40] In this case, the Wigner distribution of the complex field is transferred through the optical system in a manner such that the light field transform is merely a geometrical rotation of the Wigner distribution in the phase space. In some mathematical contexts, the optical system implements the fractional Fourier transform.[38] With the fraction Fourier transform description, the complex optical system with filters can be systematically designed and analyzed with operator mathematics.

The LCT $\mathrm{Fr}[\cdot]$ of the optical system shown in Fig. 1 takes the form

$$F(x_2,y_2,z) = \mathrm{Fr}[F(x_1,y_1,0);z] = \iint_{-\infty}^{\infty} G(x_2,y_2,x_1,y_1;z)F(x_1,y_1,0)\,dx_1\,dy_1, \tag{9}$$

where $F(x_1, y_1, 0)$ is the input field on the DOE plane (x_1–y_1 plane) and $F(x_2, y_2, z)$ indicates the 3D light field distribution in the image volume. $G(x_2, y_2, x_1, y_1; z)$ is the kernel of the forward Fresnel transform given by

$$\begin{aligned} &G(x_2,y_2,x_1,y_1;z=d_1+d_2) \\ &= \frac{-j}{\left|\lambda(d_1+d_2) - \dfrac{\lambda d_1 d_2}{f}\right|} \exp\left\{\frac{j\pi}{\lambda(d_1+d_2) - \dfrac{\lambda d_1 d_2}{f}}\left[\left(1-\frac{d_1}{f}\right)(x_2^2+y_2^2) - 2(x_2x_1+y_2y_1) + \left(1-\frac{d_2}{f}\right)(x_1^2+y_1^2)\right]\right\}. \end{aligned} \tag{10}$$

It is noted that when the focal length f of the lens is infinite, the propagator of the generalized Fresnel transform leads to the free space propagator. When the output image plane is normal to the optical axis, the inverse Fresnel transform denoted by $\mathrm{Fr}^{-1}[\cdot]$ can be expressed as

$$F(x_1,y_1,0) = \mathrm{Fr}^{-1}[F(x_2,y_2,z=d_1+d_2)] = \iint_{-\infty}^{\infty} G^{-1}(x_1,y_1,x_2,y_2;d_1+d_2)F(x_2,y_2,d_1+d_2)\,dx_2\,dy_2, \tag{11}$$

where $G^{-1}(x_1, y_1, x_2, y_2; d_1 + d_2)$ is the propagator of the inverse Fresnel transform given by

$$\begin{aligned} &G^{-1}(x_1,y_1,x_2,y_2;d_1+d_2) \\ &= \frac{j}{\left|\lambda(d_1+d_2) - \dfrac{\lambda d_1 d_2}{f}\right|} \exp\left\{\frac{-j\pi}{\lambda(d_1+d_2) - \dfrac{\lambda d_1 d_2}{f}}\left[\left(1-\frac{d_2}{f}\right)(x_1^2+y_1^2) - 2(x_2x_1+y_2y_1) + \left(1-\frac{d_1}{f}\right)(x_2^2+y_2^2)\right]\right\}. \end{aligned} \tag{12}$$

Also, we can represent the diffraction field through the optical system in the Hermite-Gaussian-mode representations as follows. Let

$$\lambda q_{\mathrm{out}} = \frac{A(-j\lambda\breve{z}) + B}{C(-j\lambda\breve{z}) + D}, \tag{13}$$

$$\frac{1}{q_{\mathrm{out}}} = \frac{1}{R_{\mathrm{out}}(d_1,d_2,f)} + \frac{j\lambda}{W_{\mathrm{out}}^2(d_1,d_2,f)}, \tag{14}$$

$$\alpha_{\mathrm{out}} = \arctan\left(\frac{B}{AW_0^2}\right), \tag{15}$$

where A, B, C, and D are defined by $A = 1 - d_2/f$, $B = \lambda(d_1 + d_2) - \lambda d_1 d_2/f$, $C = -1/(\lambda f)$, and $D = 1 - d_1/f$, respectively. Substituting eqs. (13)–(15) into eq. (5), we obtain the propagating Hermite-Gaussian-mode representation as

$$\begin{aligned} F(x, y, d_1, d_2, f) &= \mathrm{Fr}\left[\frac{1}{W_0}\psi_g\left(\frac{x'}{W_0}\right)\psi_h\left(\frac{y'}{W_0}\right)\right] \\ &= \frac{\exp[jkz]}{W_{\mathrm{out}}(d_1, d_2, f)}\psi_g\left(\frac{x}{W_{\mathrm{out}}(d_1, d_2, f)}\right)\psi_h\left(\frac{y}{W_{\mathrm{out}}(d_1, d_2, f)}\right)\exp\left[jk\frac{x^2 + y^2}{2R_{\mathrm{out}}(d_1, d_2, f)} - j(g + h + 1)\varsigma_{\mathrm{out}}(d_1, d_2, f)\right]. \end{aligned} \tag{16}$$

For practical optimization, both the field and the integral transform according to the Nquist sampling condition must be discretized. There are some fundamental limitations, such as the spatial frequency bandwidth limitations induced by the fixed optical frequency and the finite effective aperture of the optical system that generates light fields. Due to the bandwidth limitation, the light field can be sampled with a certain sampling interval. This sampling problem of the 3D light fields was thoroughly analyzed in refs. 19 and 22. When computing the diffraction field with the Fresnel transform, we can use the fast Fourier transform (FFT) algorithm for efficient calcuation. It is noted that the Hermite-Gaussian-mode expansion of the field distribution enables us to discretize only the field since the mode propagation is already obtained as shown in eqs. (6) and (7). Because of this feature, the Hermite-Gaussian-mode representation is advantageous, particularly, in the laser beam shaping problem such as the generation of 3D nondiffracting beams.[20,22,23,41] The discrete Hermite-Gaussian modes are well established. The Harper's equation[38] generates discrete Hermite-Gaussian modes with completeness and orthogonality.

3. Mathematical Modeling of Light Field Synthesis Problem

In this section, the light field synthesis problem is accounted for. At first, the definition of light field synthesis is addressed, and then, the strategies for achieving the solutions are discussed.

3.1 *Definition of light field synthesis problem*

The most fundamental question in light field synthesis is what kind of light fields can be formed in free space. Figure 2 shows a mapping between the **k**-vector domain (k_x, k_y, k_z) and the space domain (x, y, z). The **k**-vector domain is restricted to the surface of a sphere with radius of $2\pi/\lambda$. Furthermore, the **k**-vectors can exist in the small region around the k_z axis due to the constraint of the paraxial rays. Before selecting the target object, we should predict whether the target object can be expressed by the light field. When the target object does not satisfy the wave equation, the DOE design for generating the target object is, of course, nonsense. For example, the Gaussian beam is a feasible 3D structure that can be generated, but the complete non-diffracting beam having nonvarying beam width along the propagation cannot be supported in free space because the complete nondiffracting beam does not satisfy the wave equation. Furthermore, the fundamental question, "What kinds of field distribution patterns can exist in the specified 3D space domain?", cannot be answered *a priori*. The selection of the proper target object is based on expectation and trial.

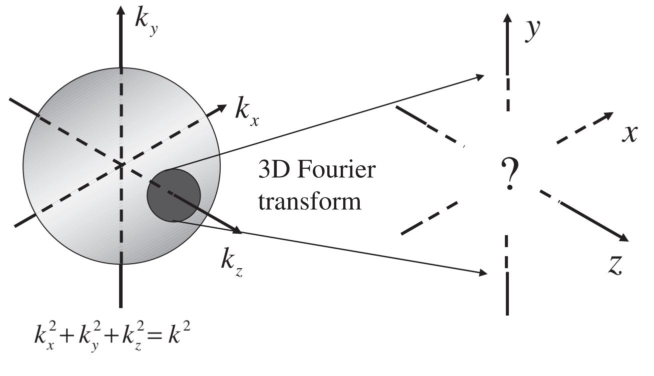

Fig. 2. Mapping from 2D paraxial k-vector surface to 3D space domain.

The field synthesis problem requires a mathematical framework for optimization. In this section, the mathematical statement of the light field synthesis problem is presented. The diffraction field generated by a DOE is represented by the LCT in the Fourier representation:

$$F(x_2, y_2, z) = \iint_{-\infty}^{\infty} G(x_2, y_2, x_1, y_1; z)A(x_1, y_1)\exp(j\phi(x_1, y_1))\,dx_1\,dy_1, \tag{17}$$

where $A(x_1, y_1)\exp(j\Phi(x_1, y_1)) = F(x_1, y_1, z = 0)$ is the complex field just after the DOE. In the ideal phase-only DOE, the amplitude $A(x_1, y_1)$ is position-independent and has a maximum value. However, in many real cases, it is somewhat dependent on the phase, i.e., it can be written as $A(x_1, y_1) = A(\Phi(x_1, y_1))$. This kind of modulation occurs in surface relief dielectric DOEs due to internal multiple reflections[31] and in liquid-crystal-phase SLMs. In the Hermite-Gaussian-mode representation, the light field on the DOE is described by

$$A(\phi(x_1, y_1))\exp(j\phi(x_1, y_1)) = \sum_{g,h} C_{gh}\frac{1}{W_0}\psi_g\left(\frac{x_1}{W_0}\right)\psi_h\left(\frac{y_1}{W_0}\right), \tag{18}$$

and its diffracted field is represented by eq. (16).

Basically, the light field synthesis problem can be classified into three categories, as indicated in Fig. 1. Figures 1(a) and 1(b) indicate the 2D domain intensity distribution synthesis problem and the 3D domain intensity distribution synthesis problem, respectively. In Fig. 1(c), the 3D image synthesis problem is shown. The intensity distribution is proportional to the absolute square of the light field in the spatial domain. That is, in most applications, we have only the desired amplitude pattern of the light field, and hence, we have a degree of freedom in choosing the phase of the light field in the output image plane (or volume). If a photosensitive medium fills the image volume, the medium can record the spatial field intensity profile. In the 3D domain intensity distribution problem, only the 3D intensity structures of the light fields in the specified spatial domain are mainly considered. The 3D image synthesis is not the simple intensity distribution synthesis in the 3D domain. In Fig. 1(c), it is indicated that different observers in different positions feel different perspectives. The 3D image synthesis requires some specific objective constraints regarding the multiple viewing directions.[42)]

For numerical computation, in both Fourier and Hermite-Gaussian mode representations, the field is discretized on computation grids. The computation grids at the input and 2D output domains are, respectively, set to

$$(x_{1,k}, y_{1,l}) = \left(\left\{-\frac{N+1}{2}+k\right\}\Delta x_1, \left\{-\frac{N+1}{2}+l\right\}\Delta y_1\right), \quad \text{for } k,l = 0,1,\ldots,N, \tag{19a}$$

and

$$(x_{2,p}, y_{2,q}) = \left(\left\{-\frac{N+1}{2}+p\right\}\Delta x_2, \left\{-\frac{N+1}{2}+q\right\}\Delta y_2\right), \quad \text{for } p,q = 0,1,\ldots,N, \tag{19b}$$

where Δx_1 (Δx_2) and Δy_1 (Δy_2) are the sampling intervals of the x-axis and the y-axis in the DOE domain (the output domain). Then, the integral of eq. (17) is discretized as

$$F_{p,q} = \sum_{k,l} G_{p,q,k,l} A(\phi_{k,l}) \exp(j\phi_{k,l}). \tag{20}$$

For convenience, the 2D notation is changed to one-dimensional notation by setting $m = (p-1)N + q$ and $n = (k-1)N + l$. Then, $F_{p,q}$, $\phi_{k,l}$, and $G_{p,q,k,l}$ are denoted by F_m, ϕ_n, and G_{mn}, respectively. Then eq. (20) reads as

$$F_m = \sum_{n=1}^{N^2} G_{mn} A(\phi_n) \exp(j\phi_n). \tag{21a}$$

This equation can be expressed in the matrix form

$$\begin{bmatrix} F_1 \\ F_2 \\ \vdots \\ F_{N^2} \end{bmatrix} = \begin{bmatrix} G_{11} & G_{12} & \cdots & G_{1N^2} \\ G_{21} & \ddots & & \\ \vdots & & \ddots & \\ G_{N^2 1} & & & G_{N^2 N^2} \end{bmatrix} \begin{bmatrix} A(\phi_1)\exp(j\phi_1) \\ A(\phi_2)\exp(j\phi_2) \\ \vdots \\ A(\phi_{N^2})\exp(j\phi_{N^2}) \end{bmatrix}. \tag{21b}$$

In the Hermite-Gaussian mode representation, using $r = (g-1)N + h$, the light field just after the DOE and the diffraction field are, respectively, represented as

$$A(\phi_n)\exp(j\phi_n) = \sum_r C_r \mathrm{HG}^{(0)}_{n,r}, \tag{22a}$$

and

$$F_m = \sum_r C_r \mathrm{HG}^{(z)}_{m,r}, \tag{22b}$$

where $\mathrm{HG}^{(z)}_{m,r}$ is defined by

$$\mathrm{HG}^{(z)}_{m,r} = \frac{\exp[jkz]}{W_{\mathrm{out}}(z)} \psi_g\left(\frac{x_p}{W_{\mathrm{out}}(z)}\right) \psi_h\left(\frac{y_q}{W_{\mathrm{out}}(z)}\right) \exp\left[jk\frac{(x_p^2 + y_q^2)}{2R_{\mathrm{out}}(z)} - j(g+h+1)\varsigma_{\mathrm{out}}(z)\right]. \tag{22c}$$

These equations become the matrix forms

$$\begin{bmatrix} A(\phi_1)\exp(j\phi_1) \\ A(\phi_2)\exp(j\phi_2) \\ \vdots \\ A(\phi_{N^2})\exp(j\phi_{N^2}) \end{bmatrix} = \begin{bmatrix} \mathrm{HG}^{(0)}_{1,1} & \mathrm{HG}^{(0)}_{1,2} & \cdots & \mathrm{HG}^{(0)}_{1,N^2} \\ \mathrm{HG}^{(0)}_{2,1} & \ddots & & \\ \vdots & & \ddots & \\ \mathrm{HG}^{(0)}_{N^2,1} & & & \mathrm{HG}^{(0)}_{N^2,N^2} \end{bmatrix} \begin{bmatrix} C_1 \\ C_2 \\ \vdots \\ C_{N^2} \end{bmatrix} \tag{23a}$$

and

$$\begin{bmatrix} F_1 \\ F_2 \\ \vdots \\ F_{N^2} \end{bmatrix} = \begin{bmatrix} \mathrm{HG}^{(z)}_{1,1} & \mathrm{HG}^{(z)}_{1,2} & \cdots & \mathrm{HG}^{(z)}_{1,N^2} \\ \mathrm{HG}^{(z)}_{2,1} & \ddots & & \\ \vdots & & \ddots & \\ \mathrm{HG}^{(z)}_{N^2,1} & & & \mathrm{HG}^{(z)}_{N^2,N^2} \end{bmatrix} \begin{bmatrix} C_1 \\ C_2 \\ \vdots \\ C_{N^2} \end{bmatrix}. \tag{23b}$$

The Haper's equation generates the orthonormal set of discrete Hermite-Gaussian transform indicated in eq. (22b). The coefficients C_r are the bridge between the input field and the output field. From eqs. (21b), (23a), and (23b), we can see that

$$\begin{bmatrix} G_{11} & G_{12} & \cdots & G_{1N^2} \\ G_{21} & \ddots & & \\ \vdots & & \ddots & \\ G_{N^2 1} & & & G_{N^2 N^2} \end{bmatrix} = \begin{bmatrix} \mathrm{HG}^{(z)}_{1,1} & \mathrm{HG}^{(z)}_{1,2} & \cdots & \mathrm{HG}^{(z)}_{1,N^2} \\ \mathrm{HG}^{(z)}_{2,1} & \ddots & & \\ \vdots & & \ddots & \\ \mathrm{HG}^{(z)}_{N^2,1} & & & \mathrm{HG}^{(z)}_{N^2,N^2} \end{bmatrix} \begin{bmatrix} \mathrm{HG}^{(0)}_{1,1} & \mathrm{HG}^{(0)}_{1,2} & \cdots & \mathrm{HG}^{(0)}_{1,N^2} \\ \mathrm{HG}^{(0)}_{2,1} & \ddots & & \\ \vdots & & \ddots & \\ \mathrm{HG}^{(0)}_{N^2,1} & & & \mathrm{HG}^{(0)}_{N^2,N^2} \end{bmatrix}^{-1}. \tag{24}$$

In the 3D domain synthesis, the matrix form is extended, from eq. (21b), to

$$\begin{bmatrix} \mathbf{F}_1 \\ \mathbf{F}_2 \\ \vdots \\ \mathbf{F}_L \end{bmatrix} = \begin{bmatrix} \mathbf{G}_1 \\ \mathbf{G}_2 \\ \vdots \\ \mathbf{G}_L \end{bmatrix} \mathbf{U}, \tag{25a}$$

where $\mathbf{F}_i = \mathbf{G}_i\mathbf{U}$ is the discrete Fresnel transform at the ith sliced image plane and is equivalent to eq. (21b). In this formulation, the simplest definition of the intensity distribution synthesis problem is the minimization of the objective function

$$E = \sum_i w_i\,\mathrm{dist}(\mathbf{F}_i, \mathbf{I}_i), \tag{25b}$$

where w_i is the weight factor, $\mathbf{I}_i$ is the target intensity pattern at the ith sliced image plane and $\mathrm{dist}(\mathbf{F}_i, \mathbf{I}_i)$ denotes the objective function for the ith sliced image plane.

3.2 *Objective functions for intensity distribution synthesis*

In the light field synthesis problem, optimization processes are inevitable. For successful optimization, the correct objective function structure, the manifestation and the utilization of degrees of freedom and stable optimization algorithms must be confirmed.

In this subsection, the objective function for intensity distribution synthesis is discussed. The abstract objective function $\mathrm{dist}(\mathbf{F}_i, \mathbf{I}_i)$ stated in the previous subsection is constructed here. The light field synthesis problem is an ill-posed problem because a solution satisfying all the constraints may not exist or, if it exists, it may not be unique. Hence, in obtaining the solutions, it is possible to control the balance of a few evaluation factors by specifically designing the objective function.

First, we inspect the objective function of the 2D domain synthesis problem. The 2D spatial domain indicates a flat image plane normal to the optical axis or an arbitrarily curved surface.[17,18] In ref. 7, Wyrowski overcame the stagnation of the classical Gerchberg–Saxton algorithm by exploiting the amplitude degree of freedom. Kotlyar *et al.* showed that Wyrowski's improved algorithm can be derived from the specified designed objective function.[8] There are several quality measures of the synthesized light field distribution. The common quality measures are mean square error (MSE), uniformity and diffraction efficiency (DE), which can be defined differently according to the specifications of individual problems.[5,6] Later, it was shown that the trade-off between diffraction efficiency and uniformity of the resulting diffraction image can be lessened by using the Tikhonov regularization technique.[14,15)]

The relationship between the light field at the DOE domain and the 2D image surface is given by eq. (21b). Then the objective function takes the form

$$\mathrm{dist}(\mathbf{F}, \mathbf{I}) = \sum_{\sigma_\mathrm{S}} ||F| - \sqrt{I}|^2 + \alpha_\mathrm{S} \sum_{\sigma_\mathrm{S}} |F|^2 + \alpha_\mathrm{N} \sum_{\sigma_\mathrm{N}} |F|^2, \tag{26a}$$

where σ_S and σ_N indicate the signal area and the noise area,[7] respectively, $\mathbf{F}$ is the designed light field pattern, $\mathbf{I}$ is the objective intensity distribution, and α_S and α_N are regularization parameters.[14] In Fig. 3, the trade-off between diffraction efficiency and uniformity of the obtained diffraction image in the iterative Fourier transform algorithm (IFTA)-based DOE design is illustrated. It is noted that as the diffraction efficiency increases, the uniformity degrades. In this design example, the objective image is a square uniform-intensity pattern, and a smaller value of uniformity means the diffraction intensity pattern is more uniform, as will be shown below.

The trade-off can be mitigated by the application of the Tikhonov regularization technique. When the first-order Tikhonov regularization form is employeed,[14] the objective function is

$$\mathrm{dist}(\mathbf{F}, \mathbf{I}) = \sum_{\sigma_\mathrm{S}} ||F| - \sqrt{I}|^2 + \alpha_\mathrm{S} \sum_{\sigma_\mathrm{S}} |F|^2 + \alpha_\mathrm{N} \sum_{\sigma_\mathrm{N}} |F|^2 + \alpha_\mathrm{D} \sum_{\sigma_\mathrm{S}} [(\partial_x |F|)^2 + (\partial_y |F|)^2], \tag{26b}$$

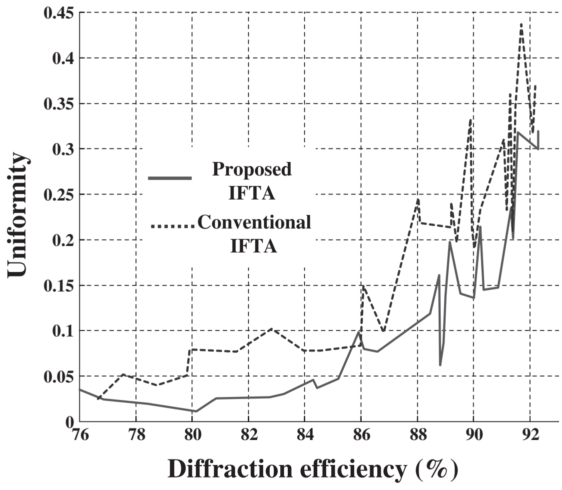

Fig. 3. Performances of conventional and proposed IFTAs with respect to the trade-off between diffraction efficiency and uniformity. The number of iterations was 100 times for both the conventional and proposed IFTAs.

where ∂_x and ∂_y denote partial derivatives with respect to x and y axes, respectively, and α_D is a regularization parameter. For general cases including gray images, the definition of the uniformity U is defined as[10)]

$$U = \frac{||F| - \sqrt{I} + \varepsilon|_{\max} - ||F| - \sqrt{I} + \varepsilon|_{\min}}{||F| - \sqrt{I} + \varepsilon|_{\max} + ||F| - \sqrt{I} + \varepsilon|_{\min}}, \quad (27)$$

where ε is the bias parameter that must be selected to make the inner terms positive ($\varepsilon > \sqrt{I} - |F|$). The measure of uniformity is indirectly but strongly related to the additional Tikhonov function in eq. (26b). In other words, the Tikhonov function is an analytic alternative for improving the uniformity. The minimization of the first derivative terms leads to improvement in the uniformity. The more explicit objective function that cannot be handled by analytic manipulation but can be handled by a numerical method takes the form

$$\begin{aligned}\mathrm{dist}(\mathbf{F}, \mathbf{I}) = \sum_{\sigma_S} ||F| - \sqrt{I}|^2 + \alpha_S \sum_{\sigma_S} |F|^2 \\ + \alpha_N \sum_{\sigma_N} |F|^2 + \eta U, \quad (28)\end{aligned}$$

where η is the weight factor of the uniformity.

In the example in Fig. 3, the trade-off is mitigated by the adaptive regularization parameter distribution (ARPD) technique, which is described in the next section. This mitigation means that at a certain diffraction efficiency, a more improved uniformity can be obtained.

A comparison of the performances of a few variants of eq. (26b) for the trade-off between the diffraction efficiency and uniformity can be found in ref. 14.

Basically, the objective function of the 3D beam-shaping problem is to determine the sliced image volume. The objective function is straightforwardly extended from eq. (26b) to the 3D domain problem as

$$\begin{aligned}\mathrm{dist}(\mathbf{F}, \mathbf{I}) = \sum_i w_i \Bigg[\sum_{\sigma_S} ||F_i| - \sqrt{I_i}|^2 + \alpha_{S,i} \sum_{\sigma_S} |F_i|^2 \\ + \alpha_{N,i} \sum_{\sigma_N} |F_i|^2 + \alpha_{D,i} \sum_{\sigma_S} [(\partial_x |F_i|)^2 + (\partial_y |F_i|)^2] \Bigg], \quad (29)\end{aligned}$$

where the subscript index i indicates the ith sliced image plane. The most important task is defining the objective function. However, the degree of freedom in the 3D domain problem is not easy to use. It is uncertain whether the target intensity distribution satisfies the 3D wave equations in free space. However, generally speaking, all areas outside the predefined signal region can be considered to be freedom areas irrespective of whether the synthesis problem is 2D or 3D.

3.3 Objective function for 3D display

A specially designed 3D field distribution can provide the realization of 3D images to observers.[42–44)] The holographic method for displaying 3D images is perceived as an ultimate solution.[45)] The CGH for generating 3D images has been considered a promising technology and has been intensively researched to overcome technological limitations.

In fact, there are several methods of floating the 3D image in free space. Figure 1(c) shows the schematic of the 3D display. The most unique property of the 3D display is that an observer sees different views of the images at different viewing positions and feels the volumetric effects of the generated 3D object images. Therefore a special objective function different from that of the intensity distribution synthesis problem is required.

There are many numerical algorithms for designing CGH for 3D display. They include the ping-pong algorithm,[46–49)] the coherent ray trace algorithm,[46)] and the diffraction specific algorithm.[50)] A recently proposed Fourier-type CGH design method with many different angular projections[42–44)] is also an important technique. In the conventional CGH design, the physical modeling of holography is employed. Then CGH is synthesized by encoding interference fringes of the diffraction field generated by a target 3D object. However, in this method, both the amplitude and phase of the reference beam(incident wave) must be modulated. If the CGH is a phase-only element, the simple interference fringe synthesis method is not appropriate. The phase-only hologram cannot be directly obtained from the interference fringe calculation. The phase-only constraint requires intensive optimization techniques and well-designed objective functions.

Since the 3D image should provide obscuration and volumetric effects, the objective function of the 3D light field distribution is not as easy or intuitive as that of the intensity distribution synthesis. To realize 3D-image properties, the specific propagation directions of a pencil of rays that pass through a focal point in free space should be controlled. The phase-only hologram synthesis trials for generating stereoscopic images or elemental images for integral imaging have been reported recently.[51–53)] Nevertheless, to our knowledge, the objective function structure for phase-only CGH generating the full-parallax 3D image synthesis problem has not been reported and requires further study. We believe one good way is to study the method of designing CGHs that would show a 2D elemental image array that reveals different perspectives assuming an imaginary 2D lens array, as shown in Fig. 4. Figure 4(a) represents the design stage of CGH for 3D images. The precalculated elemental image of the target 3D object is set to the target image for the optimization of CGH. The mathematical modeling of light field propagation from the CGH plane to the image plane through the imaginary lens array is the first task in the design. In Fig. 4(b), the display stage is shown. In the display stage, an observer can see a 3D image floating in the image volume since the light field that generates the elemental image in the image plane behind the lens array should have full parallax stereoscopic and volumetric effects in the image volume.

3.4 Mathematical methods for solving synthesis problem

The objective functions defined in the previous subsections can be minimized using the proper optimization algorithms. When selecting a numerical optimization algorithm, several factors, such as available memory, computing time, and convergence property, are taken into account. As the objective function, the most efficient iterative algorithm should be selected in the practical optimization.

The optimization methods can be categorized into iterative methods and stochastic methods. Representatives of the stochastic methods are the direct binary search

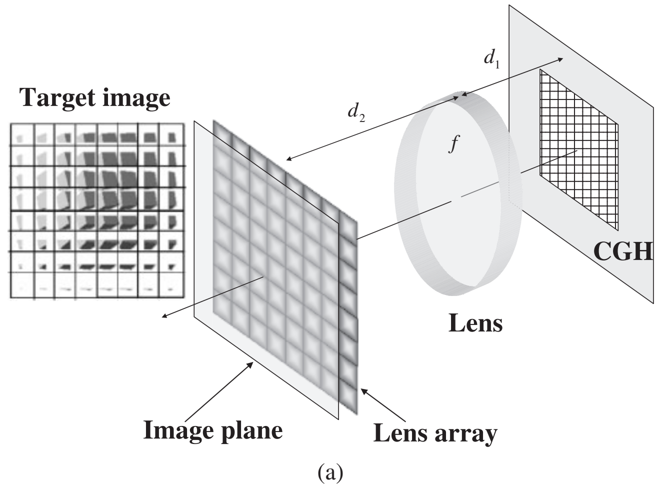

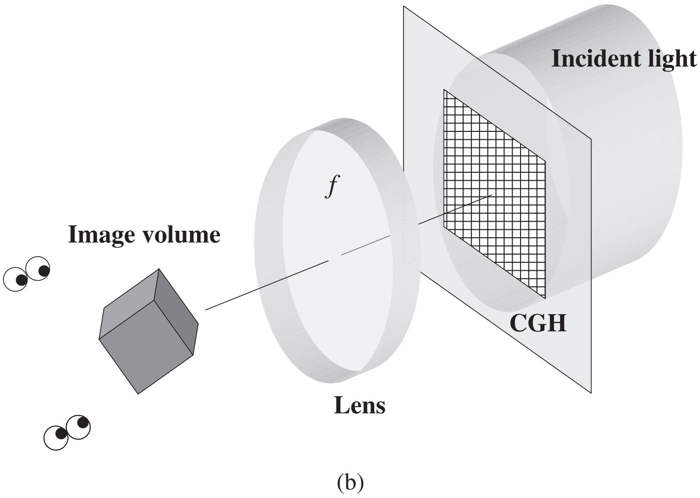

Fig. 4. (a) Design stage (recording stage) of DOE for 3D image assuming an imaginary two-dimensional lens array. The precalculated elemental image of the target 3D object is the target image for DOE optimization. (b) In the display stage, without the lens array, observers can see a 3D image floating in the image volume.

method,[54] the simulated annealing,[55] and the genetic algorithm.[56] However, in this paper, the mathematical iterative methods, the projection type optimization method and the conjugate gradient method, are mainly focused on.

3.4.1 *Iterative projection method*

Piestun and Shamir explained that many iterative methods for light field synthesis are included in the more general concept of the generalized projection or block-projection methods.[22] The iterative Fourier transform algorithm (IFTA),[7,57,58] ping-pong algorithm, input–output algorithm[4] are examples of the specific forms of the projection algorithm.

For the 2D domain intensity distribution, the iterative projection algorithm for the objective function, eq. (26a), which is called IFTA, can be derived to take the form[15]

$$\bar{F}_n = \begin{cases} \tau F_0 \exp(j\Phi_n) + \left\{1 - \tau - \tau\left[\dfrac{2\gamma}{\pi}\tan^{-1}\left(\dfrac{|F_n(x,y)| - F_0(x,y)}{F_0(x,y)}\right) + \gamma - 1\right]\right\}F_n & \text{for } (x,y) \in \sigma_{\mathrm{S}} \\ F_n & \text{for } (x,y) \notin \sigma_{\mathrm{S}} \end{cases}, \tag{30}$$

where τ is the relaxation parameter and σ_{S} indicates the signal area. See Fig. 5 for other notations. The contraint to be satisfied is that the light field must have the form of $A(\Phi(x_1, y_1))\exp(j\Phi(x_1, y_1))$ at the DOE domain. The $(n+1)$th signal F_{n+1} is obtained by applying the error-reduction operator as

$$F_{n+1} = \mathrm{Fr}[D_{\mathrm{DOE}}[\mathrm{Fr}^{-1}[\bar{F}_n]]], \tag{31}$$

where $\mathrm{Fr}[\cdot]$ denotes the Fresnel transform and the operator $D_{\mathrm{DOE}}[\cdot]$ expresses the surface boundary condition in the DOE plane as

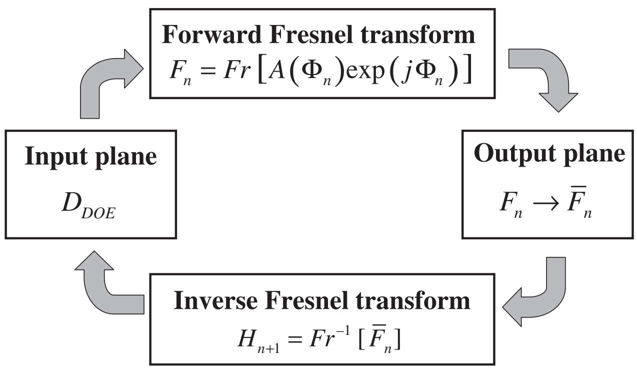

Fig. 5. Diagram of iterative Fourier transform algorithm.

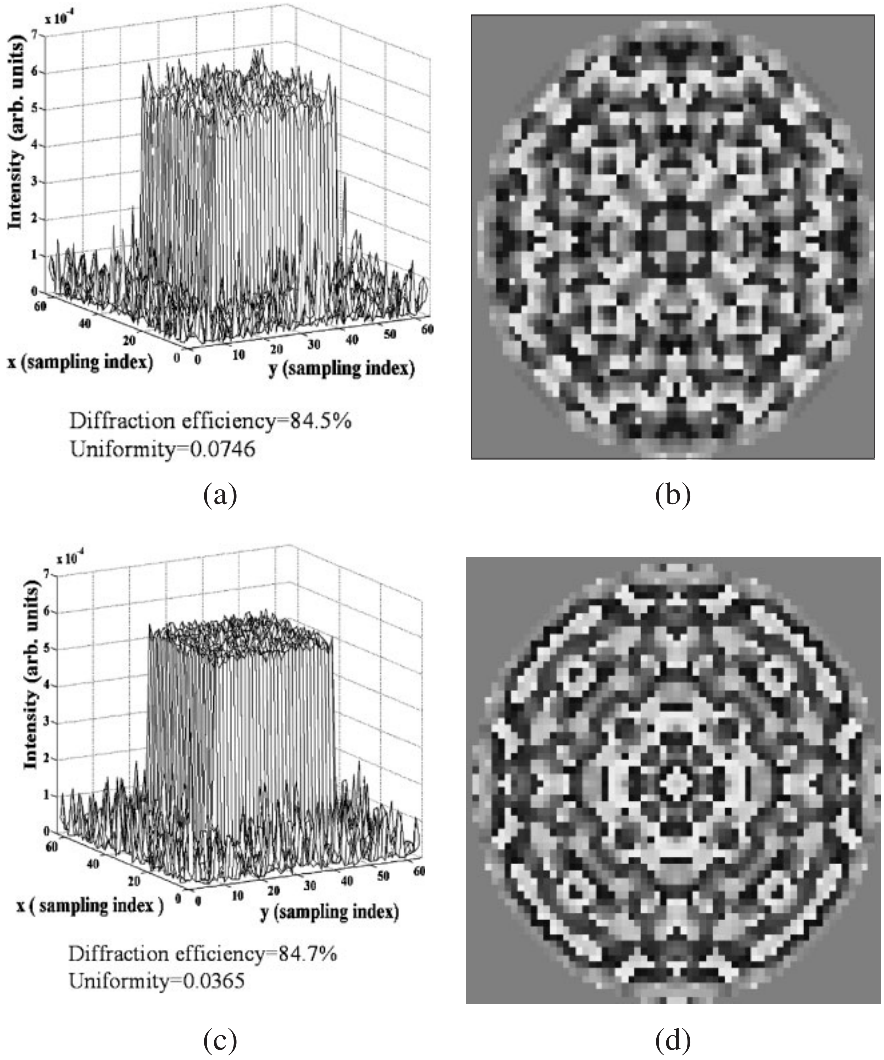

Fig. 6. (a) Intensity distribution of the square image generated by the DOE with (b) the phase profile obtained using the conventional IFTA. (c) Intensity distribution of the square image generated by the DOE with (d) the phase profile obtained by the IFTA with ARPD.[15)]

$$D_{\mathrm{DOE}}[H] = \begin{cases} A(\arg(H))\exp[j\arg(H)] & (u,v) \in \Omega \\ 0 & (u,v) \notin \Omega \end{cases}, \tag{32}$$

where Ω denotes the encoding area in the DOE plane and $\arg(H)$ is the phase function of the complex function H. The iterative algorithm described with eqs. (30) and (31) is shown schematically in Fig. 5. The form of IFTA is equipped with the ARPD that modifies the diffraction image adaptively according to the difference, $|F_n(x,y)| - F_0(x,y)$, as shown in eq. (30). Figure 6 shows the intensity distributions of the diffraction images generated by the DOE designed with the simple objective function and with the objective function with the ARPD.[15)] An improved algorithm derived from the objective function of eq. (26b) is expressed as[14)]

$$\bar{F}_n = \begin{cases} \tau F_0 \exp(j\Phi_n) + \left\{1 - \tau - \tau\left[\dfrac{2\gamma}{\pi}\tan^{-1}\left(\dfrac{|F_n(x_2,y_2)| - F_0(x_2,y_2)}{F_0(x_2,y_2)}\right) + \gamma - 1\right]\right\}F_n + \tau\alpha_{\mathrm{D}}\nabla^2|F_n|\exp(i\psi_n) & \text{for } (x_2,y_2) \in S \\ (1 - \tau\alpha_{\mathrm{N}})F_n & \text{for } (x_2,y_2) \notin S \end{cases}. \tag{33}$$

This algorithm is devised to improve the mitigation of the trade-off between diffraction efficiency and uniformity. The numerical results related to these algorithms can be found in ref. 14. Figure 7 shows examples of the 2D domain intensity distribution synthesis using the IFTA.[9)] This figure shows that the aperture shape of the DOE is another design factor in the generation of diffraction images without phase dislocations. Many phase dislocations appear in the resulting diffraction image with the circular aperture DOE, as indicated in Figs. 7(a) and 7(b). However, the modification of the aperture shape, as in Fig. 7(c), leads to the elimination of phase dislocations as shown in Fig. 7(d).

While the problem of generating arbitrarily patterns on one plane is well established, the 3D domain intensity

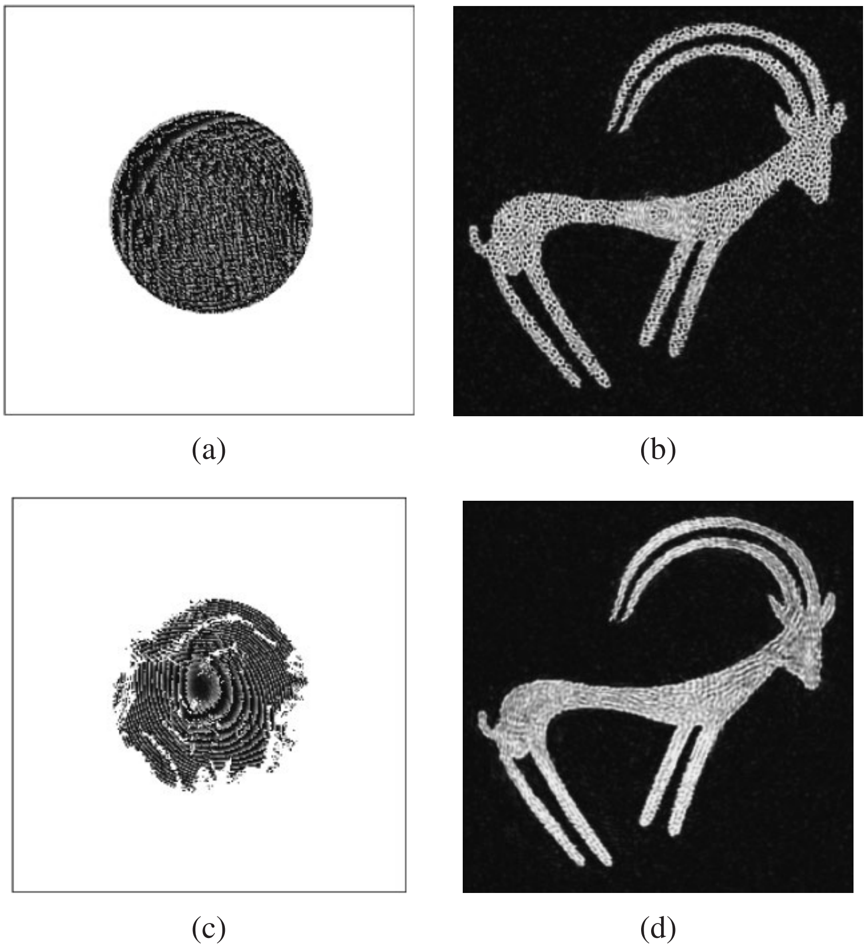

Fig. 7. (a) Phase profile of the conventional DOE with no aperture apodization and (b) its generated diffraction image revealing some phase dislocations. (c) Phase profile of the DOE with apodized aperture and (d) its resulting diffraction image without phase dislocations.[9)]

distribution synthesis problem had not been tackled until recently. Piestun *et al.* proposed a parallel block-projection scheme to minimize eq. (25b). Its feasibility was shown in several works.[19–22)] In the 3D domain intensity distribution synthesis problem, the iterative parallel projection method is used. In this method, at each iteration stage, diffraction images at all sectioned output planes are improved by the multiple use of the 2D algorithm. In particular, the Hermite-Gaussian-mode representation is appropriate for the 3D beam-shaping problem. An interesting example of 3D light field synthesis for a propagation-invariant rotating beam based on the Hermite-Gaussian-mode representation can be found in ref. 22.

3.4.2 Nonlinear conjugate gradient method

When, fortunately, the analytic form of the inverse transform exists, without the heavy burden of numerically computing the inverse matrix, we can run the iterative 2D projection algorithm using FFT. When the image surface is arbitrarily curved, the 3D projection algorithm is needed. However we can use another and somewhat direct optimization methods such as the nonlinear conjugate gradient method (NCGM)[59)] with the 2D-domain model. The output surface is represented by the defocus distribution $s(x_2, y_2)$ in the x_2y_2z coordinate, as shown in Fig. 8(a). Then the relationship between the DOE plane and the output plane can be represented by adding the output surface profile $s(x_2, y_2)$ to d_2 in eqs. (9) and (10). Therefore, the forward propagation transform exists, but the analytic form for the inverse propagation transform does not exist because of the non-invertible property of the forward transform. In this case, the projection-type algorithm should be a 3D algorithm. Also, the numerically forced inversion of the forward transform uses much memory.

The NCGM provides a more general treatment than the projection method for the generalized objective function of eq. (29) as well as the 2D objective function of eq. (26a). Let the objective function be the weighted MSE as

$$\mathrm{dist}(\mathbf{F}, \mathbf{I}) = \sum_{m} \left[w(m) \left| \sum_{n} G_{mn} A(\phi_n) \exp(j\phi_n) \right| - \sqrt{I_m} \right]^2, \tag{34}$$

where eq. (21a) is substituted into eq. (26a) with α_{S} and α_{N} set to zero. In the NCGM procedure, the obtained result reflects the structure of the specified weight factor distribution $w(m)$ precisely. By default, the weight distribution $w(m)$ is structured by $w(m) = 1$ for $I(m) \neq 0$, and $w(m) = 0$ for $I(m) = 0$. The key in the NCGM is the calculation of the gradient vector of the objective function. Let the function M_m be defined as

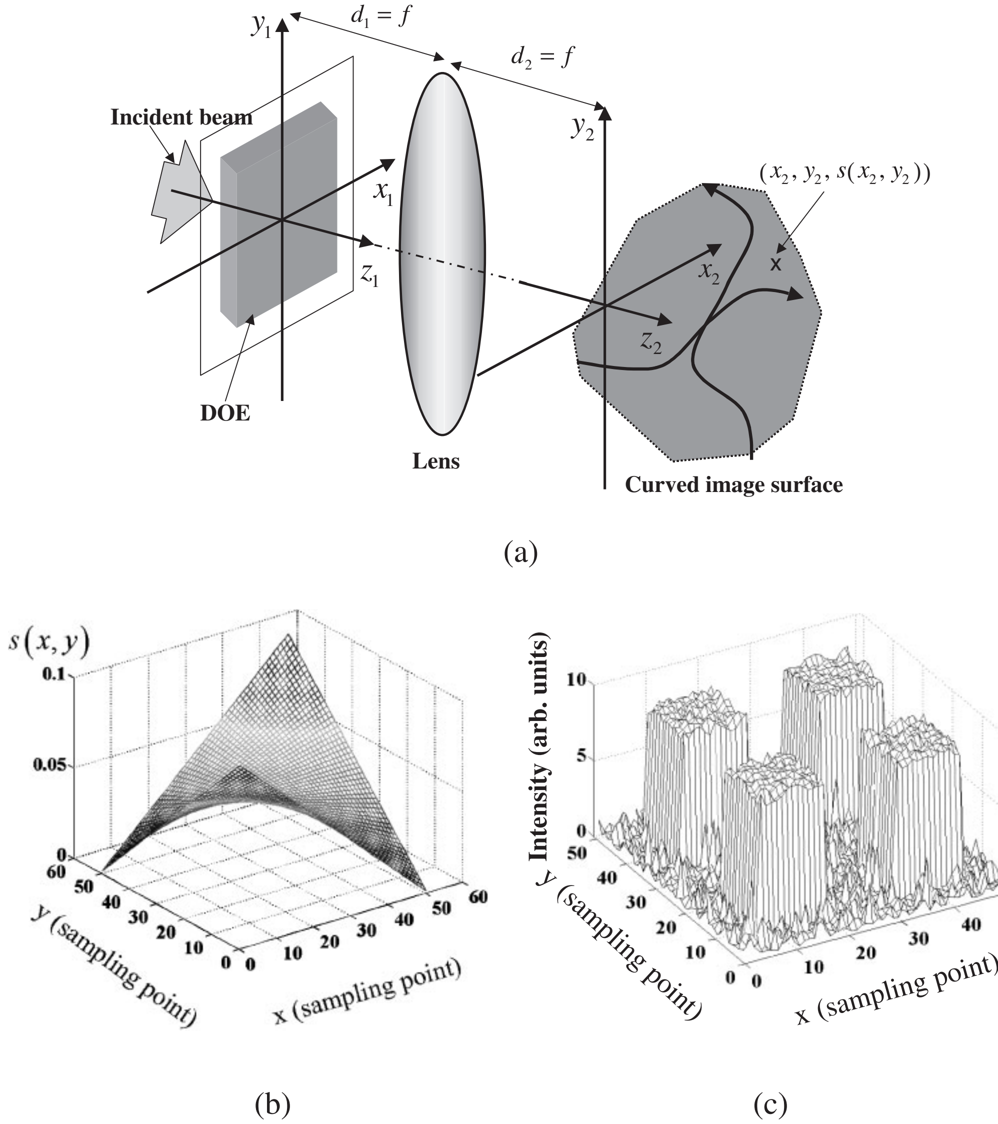

Fig. 8. (a) Problem of forming a desired diffraction image on an arbitrarily curved surface. (b) Example of a curved (defocus) surface $s(x, y)$. (c) Intensity distribution on the curved output surface of the diffracted field generated by the DOE optimized by the NCGM.

$$M_m = \left| \sum_{n=1}^{N^2} G_{mn} A(\phi_n) \exp(j\phi_n) \right|^2 . \tag{35}$$

The gradient vector of the objective function $\mathrm{dist}(\mathbf{F}, \mathbf{I})$ takes the form

$$\nabla \mathrm{dist}(\mathbf{F}, \mathbf{I}) = \left[\frac{\partial \,\mathrm{dist}}{\partial \phi_1}, \frac{\partial \,\mathrm{dist}}{\partial \phi_2}, \ldots, \frac{\partial \,\mathrm{dist}}{\partial \phi_n} \right], \tag{36}$$

where each component $\partial \,\mathrm{dist}/\partial \phi_n$ is given by

$$\frac{\partial \,\mathrm{dist}}{\partial \phi_n} = \sum_{m=1}^{N} \left(1 - \frac{I_m}{\sqrt{M_m}} \right) \frac{\partial M_m}{\partial \phi_n}, \tag{37a}$$

where $\partial M_m/\partial \phi_n$ is obtained as

$$\begin{aligned} \frac{\partial M_m}{\partial \phi_n} &= 2|G_{mn}|^2 A(\phi_n) \frac{\partial A(\phi_n)}{\partial \phi_n} \\ &\quad + 2\,\mathrm{Re}\left[\frac{\partial A(\phi_n)}{\partial \phi_n} \exp(j\phi_n) G_{mn} (F_m^* - G_{mn}^* A(\phi_n) \exp(-j\phi_n)) \right] \\ &\quad - 2\,\mathrm{Im}[A(\phi_n) \exp(j\phi_n) G_{mn} (F_m^* - G_{mn}^* A(\phi_n) \exp(-j\phi_n))], \end{aligned} \tag{37b}$$

where $\mathrm{Re}[\cdot]$ and $\mathrm{Im}[\cdot]$ indicate the real part and the imaginary part of complex number, respectively. In the standard NCGM, the DOE phase profile $\mathbf{\Phi}_k$ can be obtained by the following iteration procedure. The phase profile $\mathbf{\Phi}_k$ at the $(k+1)$th iteration stage is updated through the form

$$\mathbf{\Phi}_{k+1} = \mathbf{\Phi}_k + \tau_k \mathbf{d}_k, \quad \text{for } k = 0, 1, 2, \ldots \tag{38}$$

where τ_k and $\mathbf{d}_k$ denote the step size and the search direction vector, respectively, at the $(k+1)$th iteration stage. The search direction vector $\mathbf{d}_k$ is given by

$$\mathbf{d}_k = -\nabla \mathrm{dist}(\mathbf{F}(\mathbf{\Phi}_k), \mathbf{I}) + \beta_{k-1} \mathbf{d}_{k-1}, \tag{39}$$

where the Fletcher–Reeves formula is used to set β_{k-1} to

$$\beta_{k-1} = \frac{|\nabla \mathrm{dist}(\mathbf{F}(\mathbf{\Phi}_k), \mathbf{I})|^2}{|\nabla \mathrm{dist}(\mathbf{F}(\mathbf{\Phi}_{k-1}), \mathbf{I})|^2}. \tag{40}$$

The step size τ_k is determined to minimize the objective function $\mathrm{dist}(\mathbf{F}(\mathbf{\Phi}_{k+1}), \mathbf{I})$ with the aid of the bracketing algorithm and the golden section search algorithm.[59)]

Figures 8(b) and 8(c) show an example of DOE design using the NCGM. It is assumed that the diffraction image is formed on an arbitrarily curved surface, as shown in Fig. 8(b). The resulting intensity distribution on the curved output surface of the diffracted field generated by the DOE optimized by the NCGM is shown in Fig. 8(c). Another example of axial-intensity distribution synthesis with the NCGM can be found in ref. 60.

4. Diffractive Optic Analysis for Subwavelength DOEs and Surface Plasmon Polaritons

In this section, rigorous diffractive optic analysis methods for subwavelength DOEs and surface plasmon polaritons are described.

The diffraction phenomena in the subwavelength and nanoscale optical regime are not trivial and will not lead to the usual results expected from a simple diffraction grating theory. These restrictions of diffraction-limited optics in the subwavelength diffraction regime have been a crucial constraint in nanoscale optical imaging, sensing and nanophotonic circuit applications. Recently, they have been increasingly focused on and are playing important roles in nanoscale sciences and biophotonic applications.

These diffraction phenomena can be rigorously analyzed by electromagnetic methods that can be classified into two classes. The first is frequency domain methods and the second is space domain methods. In the frequency domain method, the electromagnetic field and the structures of the permittivity $\varepsilon(r)$ and permeability $\mu(r)$ are represented in Fourier space. As a result, the Maxwell equation is solved in Fourier space. The rigorous coupled wave analysis (RCWA) method[35–37,61,62] and Fourier modal analysis method[63,64] are representatives of frequency domain methods. The scattering matrix method (S-matrix method)[65] is usually combined with the RCWA for analyzing multi-layered structures. The finite difference time domain (FDTD) method is representative of time domain methods.[66] In the FDTD, the Maxwell equation is solved in space time by the discretization.

Figure 9 shows two binary subwavelength grating structures and their wavefront modulation characteristics analyzed by the RCWA. In Figs. 9(a) and 9(b), two comparable subwavelength grating structures are shown. The grating structure in Fig. 9(a) has a different fill factor in each cell and the grating structure in Fig. 9(b) has a different fill factor and tilt angle varying in each cell. The phase distribution of the y-component of the electric field E_y and the amplitude distribution of the electric field E_x modulated by the grating structure in Fig. 9(a) are illustrated in Figs. 9(c) and 9(e), respectively. The phase and amplitude distributions modulated by the grating structure in Fig. 9(b) are shown in Figs. 9(d) and 9(f), respectively. We can see that the fill factor and the tilt angle modulate the phase and the amplitude of the incident optical wave, respectively. In Figs. 10(a) and 10(b), the phase modulations and the amplitude modulations for several values of the fill factor and the tilt angle are shown. We can obtain wide ranges of phase and amplitude modulations by adjusting the fill factor and the tilt angle by using different subwavelength binary gratings.

It is well known that metallic subwavelength structures generate and support surface plasmon polaritons. A surface plasmon polariton is an electromagnetic surface-bound wave (p-polarized, transverse-magnetic) propagating along the interface between metal and dielectric layers. The metal behaves like a plasma, having equal amounts of positive and negative charges, of which the electrons are mobile. The bound wave has an evanescent field, which decays exponentially perpendicular to the surface. It can be produced by photons in the well-known Kretchmann–Raether attenuated total reflection (ATR) device. Surface plasmons have played a significant role in a variety of areas of fundamental and applied research[67,68] (from surface-sensitive sensors[69] to surface plasmon resonance microscopy[70]), surface plasmon resonance technology,[71] and a wide range of photonic applications.[72]

For source beam modeling, we use the angular spectrum representation and the Fourier representation of temporal pulses. For the structure analysis, the RCWA and the S-matrix method are used. Let us briefly explain the source beam modeling. A pulsed Gaussian beam with the beam radius of σ and the pulse duration of T can be represented by the following angular spectrum representation:

$$E(x,y,z,t) = \hat{x}E_x + \hat{y}E_y + \hat{z}E_z, \tag{41a}$$

where (E_x, E_y, E_z) is given by

$$\begin{aligned}(E_x, E_y, E_z) = {} & \frac{1}{T}\int_{-\pi/T}^{\pi/T} \frac{\sigma^2}{2\pi}\left(\frac{\omega}{c}\right)^2 A_t(\omega)e^{-j\omega t} \\ & \times \left[\int\!\!\int_{\alpha^2+\beta^2<1} (A_x\hat{x} + A_y\hat{y} + A_z\hat{z}) \right. \\ & \times \exp\left(-\frac{1}{2}\left(\frac{\omega}{c}\right)^2 \sigma^2(\alpha^2+\beta^2)\right) \\ & \left. \times \exp\left(j\frac{\omega}{c}(\alpha x + \beta y + \sqrt{1-\alpha^2-\beta^2})\right) d\alpha\, d\beta \right] d\omega \end{aligned} \tag{41b}$$

Here, A_x, A_y, and A_z must satisfy the plane wave condition

$$\alpha A_x + \beta A_y + \sqrt{1-\alpha^2-\beta^2}A_z = 0. \tag{41c}$$

Figure 11(a) shows the surface plasmon resonantly excited at a dielectric–metal boundary by a 3D finite Gaussian beam. The metal thickness, the beam radius, the incidence angle and the material refractive index are set to 40 nm, 2 µm, 46.41°, and 1.46, respectively. The propagation length of the plasmon wave is measured to be more than 20 µm. It is shown that the damping radiation loss as well as the ohmic loss on the metal surface is a dominant loss factor. Figure 11(b) shows the pulsed surface plasmon resonantly excited by a 3D finite Gaussian pulse. The pulse width and the pulse period are set to 2 and 5 fs, respectively. The pulsed damping radiation as well as the pulsed surface plasmon can be observed in Fig. 11.

The FDTD method, as a time-domain computational solution of Maxwell equations, is also a powerful full-vector computation method for the Maxwell equations. The FDTD method has also been widely used for analyzing the electromagnetic phenomena throughout the entire range from microwave to X-ray optics. Figure 12 shows an FDTD simulation result of a poly(methyl methacrylate) (PMMA)-based metal lamellar grating structure. A thin metal coating is deposited on the PMMA lamella binary grating structure. We believe that this PMMA–metal grating structure can be

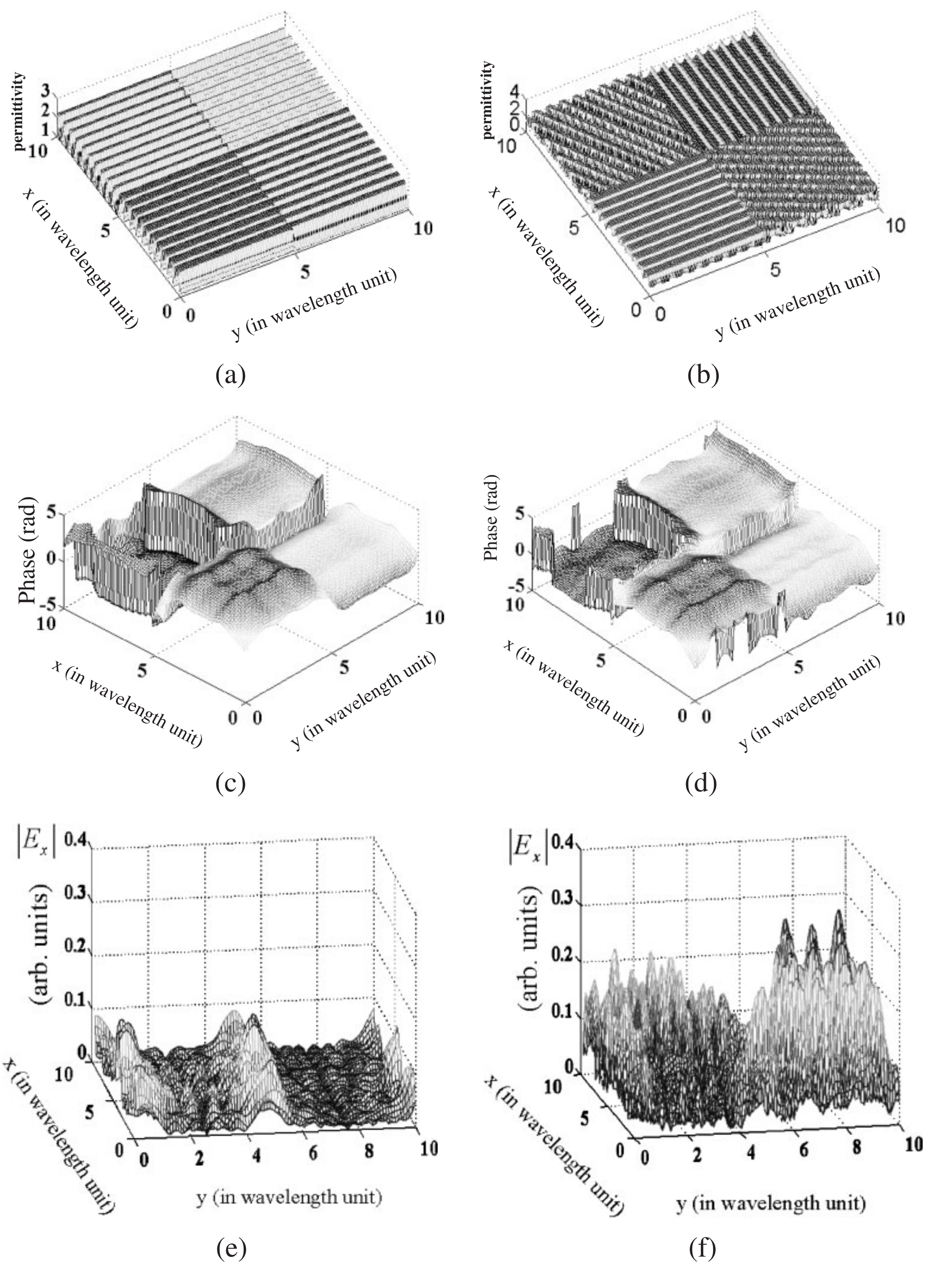

Fig. 9. (a) Grating structure with various fill factors. (b) Grating structure with various fill factors and tilt angles. (c) Phase distribution of E_y modulated by the grating shown in (a). (d) Phase distribution of E_y modulated by the grating shown in (b). (e) Amplitude distribution of E_x modulated by the grating shown in (a). (f) Amplitude distribution of E_x modulated by the grating shown in (b).

applied as a polarization-dependent multiple beam splitter and combiner with surface plasmon resonance (SPR) excitation.

5. Applications

These days, diffractive optics applications are rapidly advancing in information technologies (IT), nanotechnologies (NT), and biotechnologies (BT). The developments of computers and of semiconductor lithography technologies have made it possible to calculate and fabricate increasingly complicated DOEs. Some rapidly growing branches of diffractive optics applications are bio-optical information processing, subwavelength-scale near-field optical imaging and plasmonics, nanofabrication, and high-capacity optical data pickup/storage. Figure 13 shows some examples of DOEs in a grating-based DNA chip structure,[73,74] dynamic holographic optical tweezer system,[75,76] and high-capacity multilayered diffractive optical data pickup device.[77,78] Diffractive optics also has many industrial applications, such as in a laser beam splitter/combiner,[79] Gaussian laser beam pattern generator,[80,81] and input/output beam coupler for optical fiber communication.[82,83] Some multiple beam

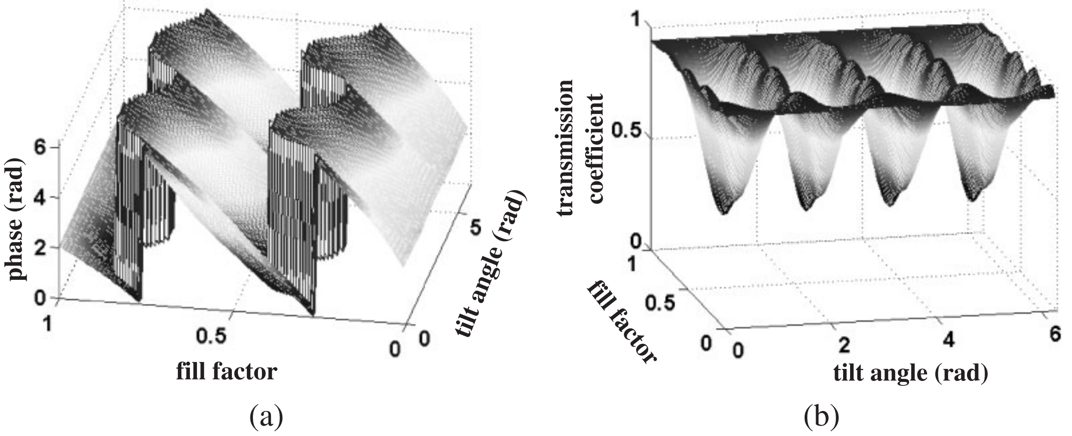

Fig. 10. (a) Phase modulations and (b) amplitude modulations for several values of fill factor and tilt angle.

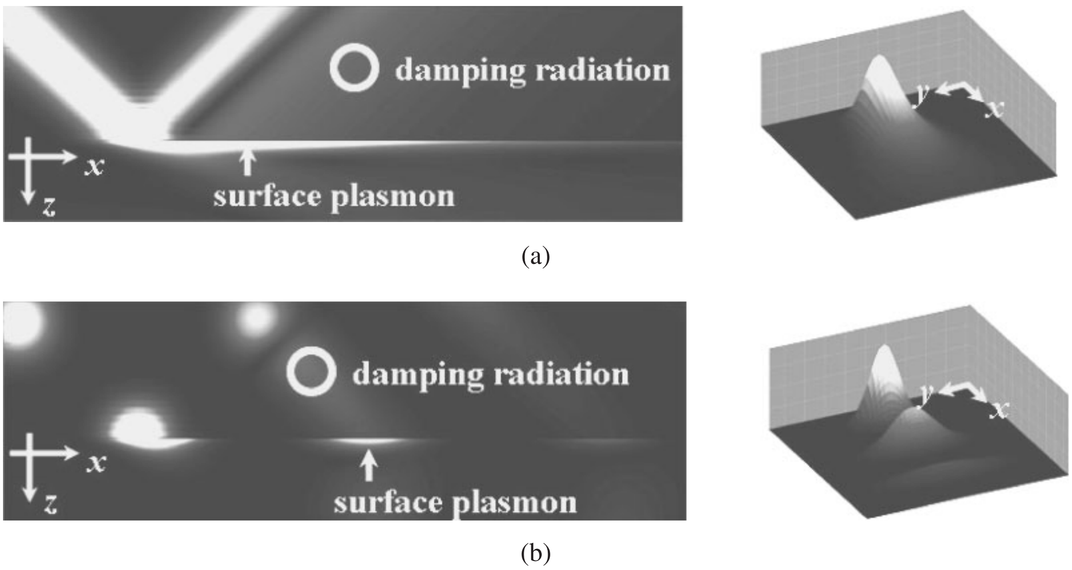

Fig. 11. (a) Resonant excitation of surface plasmon by a finite Gaussian beam. (b) resonant excitation of pulsed surface plasmon by a finite Gaussian pulse.

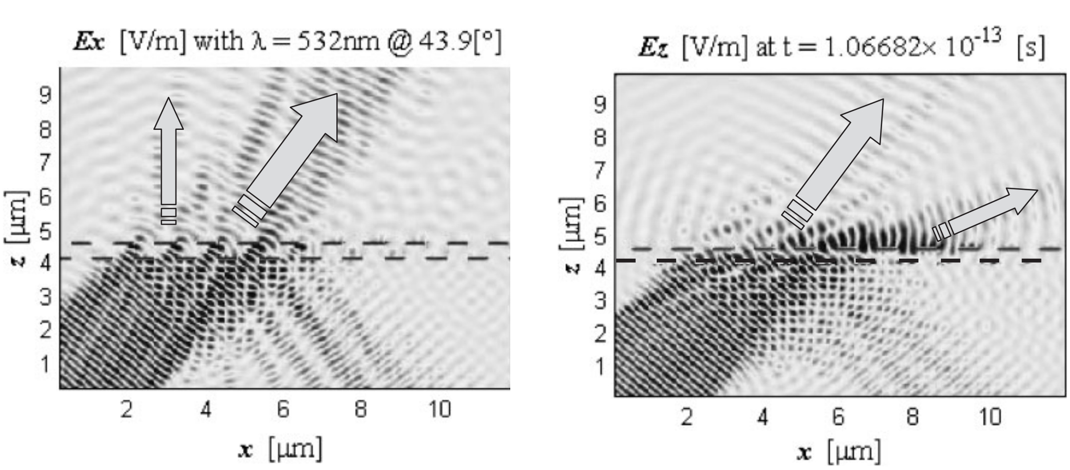

Fig. 12. FDTD simulation result of a PMMA-based metal lamellar grating structure. The following parameters were used in the calculations. The dielectric constant of the SiO_2 prism was 2.1316. The plasma frequency and collision frequency were 1558 THz and 978 THz for the incident wavelength of 532 nm, respectively. The period of the metal lamellar grating was 1061 nm and the dielectric constant of the PMMA layer was 2.2201.

splitters are useful in high-power laser material processing.[84] Other industrial applications include solar cells and precision alignment applications in space-optic technologies.[85–87] In IT, it is possible to use DOEs in different ways. Apart from classical applications in optical spatial filtering,[88–90] DOEs can be used as acousto-optic[91] or electro-

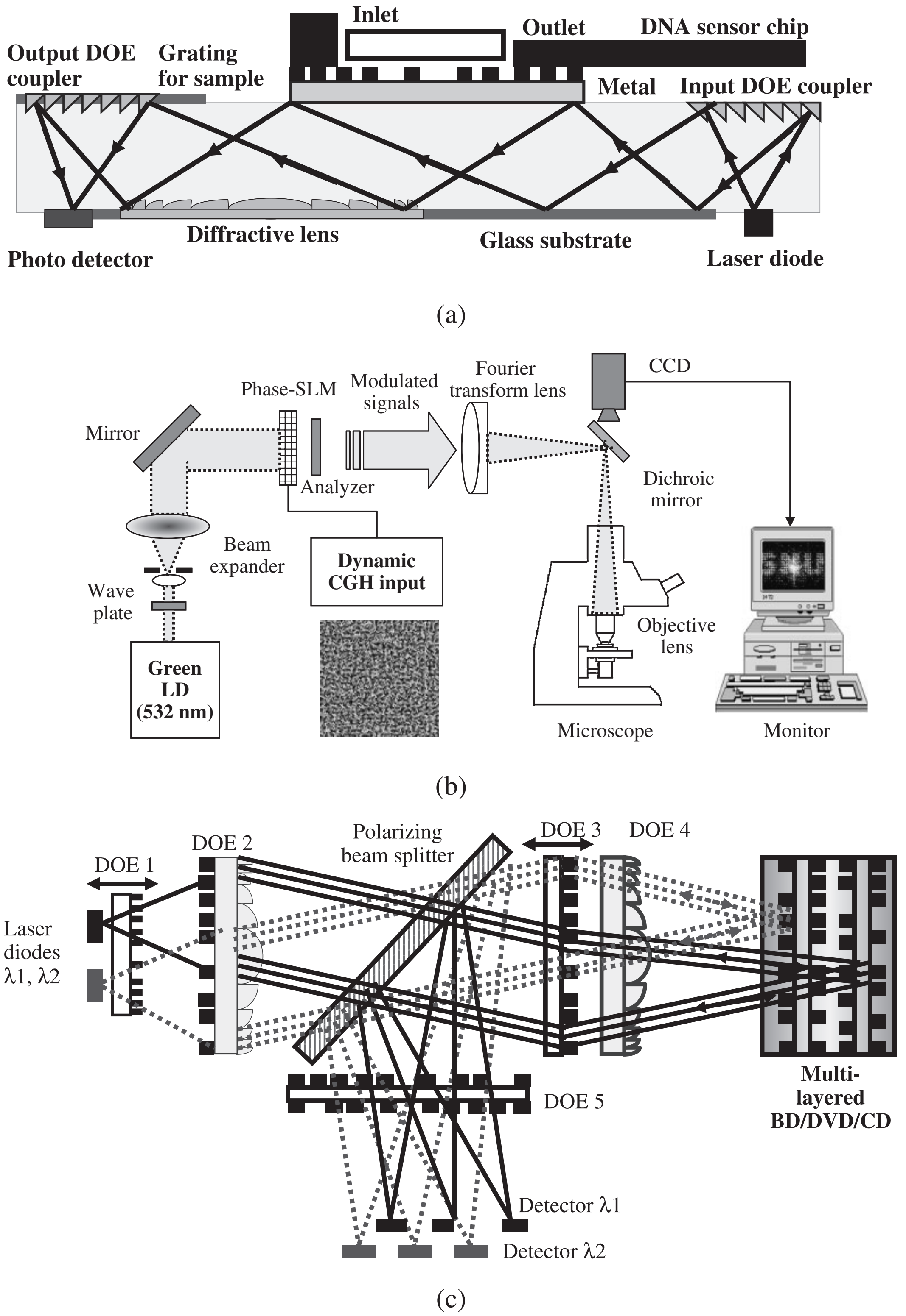

Fig. 13. Examples of DOEs in (a) grating-based DNA biochip structure,[73,74)] (b) dynamic holographic optical tweezer,[75,76)] and (c) multilayered optical pickup device.[77,78)]

optic[92)] diffractive elements in optical signal processing, real-time optical pattern correlation, and optical interconnection or wavelength division multiplexing in optical communication and computing.[93–98)]

In the following subsections we discuss some examples of diffractive optics applications.

5.1 Dynamic modulation for IT

The need for reconfigurable optical components is ever increasing in optical computing and communication systems to efficiently handle the dynamic optical functions in 3D display, optical interconnection, switching, filtering, and computing logic operation. The advances in liquid crystal (LC) materials and very large scale integration (VLSI)

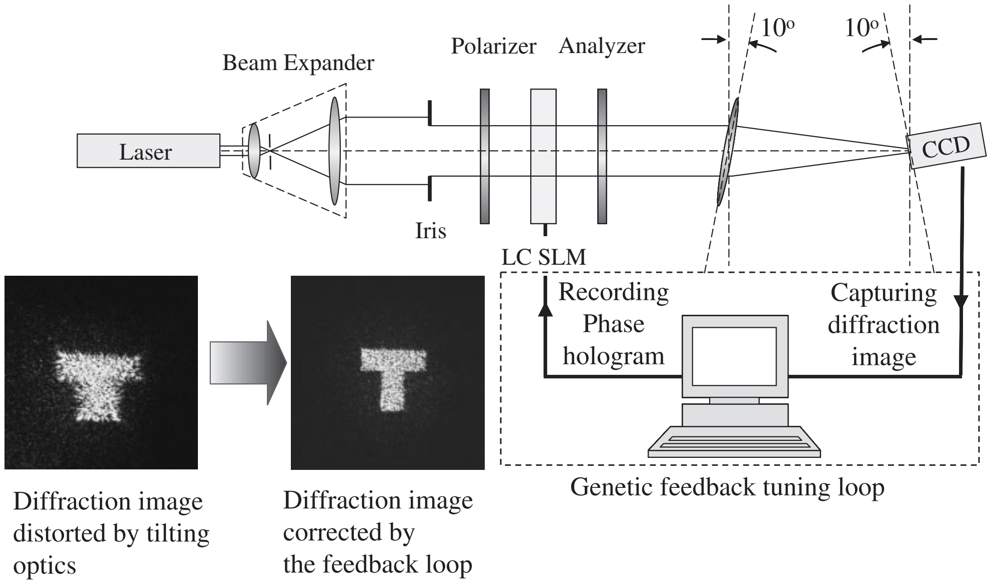

Fig. 14. The configuration of the SLM light field synthesis system with the genetic feedback tuning loop for compensating the internal aberration or misalignment of the optical system.[106]

technology have enabled the development of multiphase SLMs that can enable high-resolution, dynamic optical beam positioning, shaping, and imaging.[99] Now, 2D amplitude- and phase-type SLMs are commercially available (for example, Hamamatsu PPM8267 and Holoeye LC2002).

Recently, a reconfigurable optical interconnection system (OCULAR-II) and a holographic optical switching system (ROSES) have been demonstrated using the LC-SLMs.[100,101] Much research on an optical perfect-shuffle network system (PSNS) has been proposed and some were implemented using the multistage interconnection network systems composed of light source arrays and classical refractive, reflective, and diffractive elements.[102–104] However, these elements present the disadvantages of high cost, large element volume, heavy weight, limited flexibility, and low energy efficiency. The availability of reconfigurable interconnects can greatly improve the ability of the optical PSNS to perform different tasks. Such components can also reduce the number of active switching-element arrays and eliminate the light source array. When a phase-only material is used, the energy loss can be greatly reduced. Therefore, the holographic phase elements will have potential applications in parallel optical computing and communication systems. The multiplexed phase holograms have an advantage that multiple and complex optical functions can be superimposed in same element. For this reason, we proposed and implemented a dynamically reconfigurable optical single-stage PSNS using only one phase-type SLM with optimized high-performance multiplexed phase holograms.[105]

High-precision alignment and aberration compensation are fundamental requirements for implementing light field synthesis with SLM. Using the dynamic property of the SLM, adaptive tuning and aberration compensation can be achieved. Figure 14 shows the genetic feedback tuning loop that was proposed by us.[106] The initial phase profile is calculated with a design algorithm such as IFTA, which does not take the internal misalignment and aberration into account. However, if the optical system has misalignment or aberration, the resulting diffraction image is distorted, as indicated in Fig. 14. We proposed the feedback loop structure shown in Fig. 14, in which the genetic algorithm is employed for optimizing the Zernike polynomial phase profile to compensate the aberration of the optical system. In the system in Fig. 14, we intentionally applied 10° rotations to the lens and charged-coupled device (CCD) camera to prove robustness against misalignment. The gradual compensation by the genetic algorithm in the feedback loop results in a corrected diffraction image, as indicated in Fig. 14. This genetic feedback tuning loop can be a fundamental technique for implementing a high-precision dynamic light field synthesis system with SLM.

Also, the dynamic phase-type SLM can be used for 3D display systems such as some electro-holography systems. Recently, we proposed and implemented a dynamic full-color autostereoscopic 3D display system using color-dispersion compensated (CDC) synthetic phase holograms (SPHs)[52] and a full parallax viewing-angle-enhanced CGH 3D display system using an integral lens array and single-phase-type SLM.[51] These schemes may have advantages in cost-effectiveness, high light source utilization efficiency, and controllable color fidelity without the use of any color filters. The CDC SPHs designed for elemental image reconstruction were experimentally implemented using a simple Fourier optics system employing a phase-type SLM, two laser diode sources (for color 3D image display), an achromatic lens, a projection lens module, and an integral lens array. Figure 15 shows the optical setup of a full-color multiviewer dynamic stereoscopic system adopting a single SLM.

5.2 *Diffractive optics for dynamic 3D laser writing*

The direct laser writing technique has many advantages over the electron-beam writing technology for the fabrication of large DOEs on an arbitrary 3D surface with precise alignment. Some well-known characteristics are fast proc-

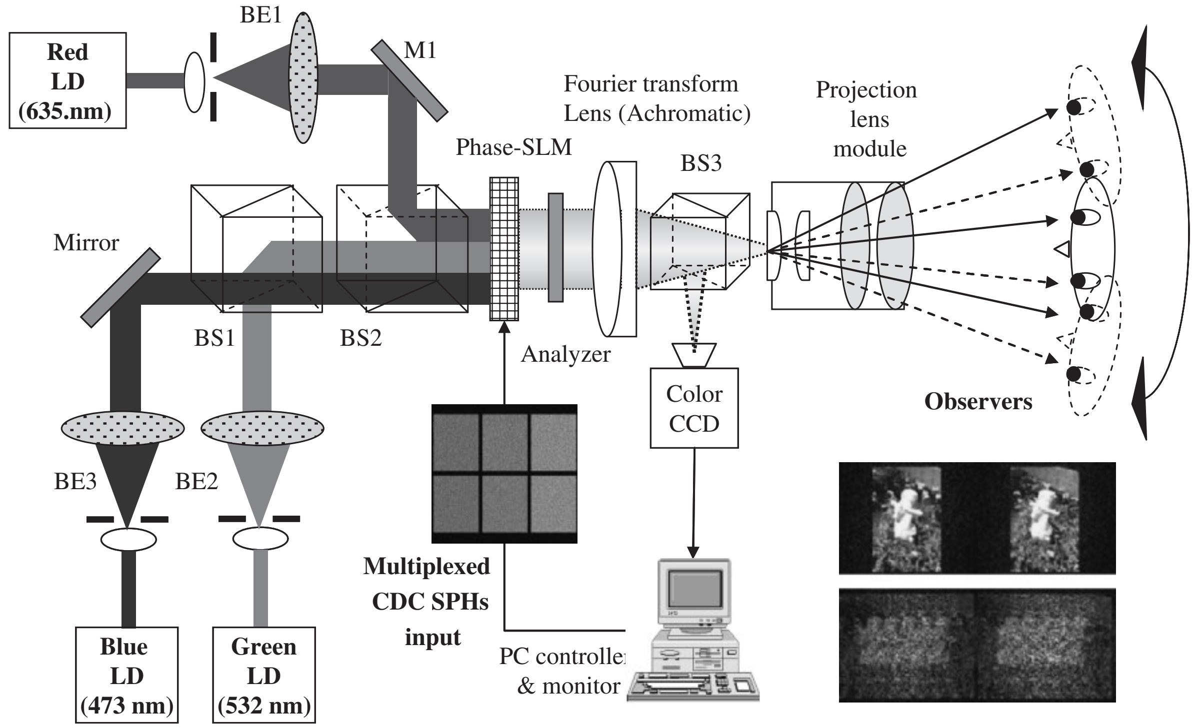

Fig. 15. Optical setup and experimental result of a full-color dynamic multiview stereoscopic system adopting a single SLM. BE, BS, LD, and M denote beam expander, beam splitter, laser diode and mirror, respectively.

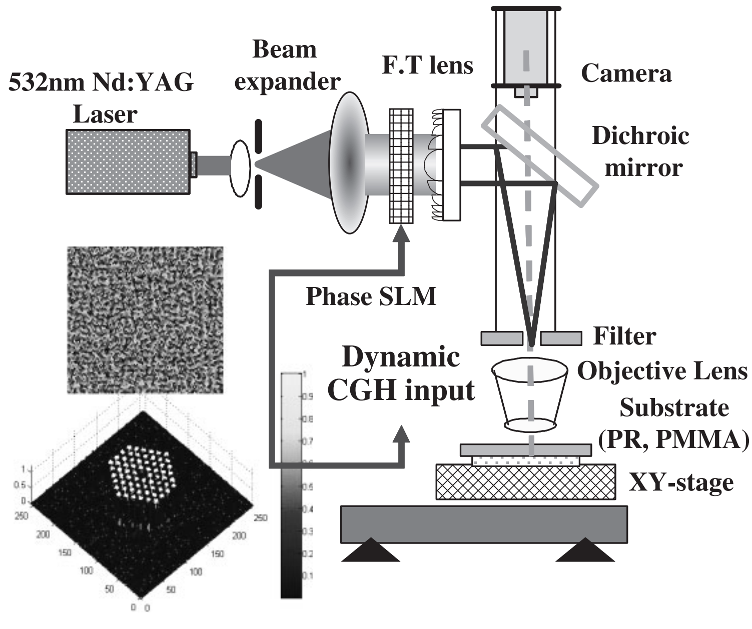

Fig. 16. High-resoultion reconfigurable laser writing system using CGH on a phase-type SLM.

essing, low fabrication cost without the need for clean room facility, simplicity and excellent fabrication quality. The prime advantage of the direct laser writing technique is that it is a maskless lithographic process. The direct laser writing technology can be further developed to allow the generation of massive parallel writing beams for mass production. Direct laser writing systems have been well described by Gale *et al.*[107–109] The "Laser Writer III" (CSEM) is based on a high precision *xy* raster scan of the photoresist-coated substrate under a focused HeCd laser beam of wavelength 442 nm. The raster scan is performed by a roller-bearing *xy*-stage with a dynamic line-positioning accuracy of about 35 nm rms. The laser writing spot is generated by a modified CD reader autofocus optics which produces a spot with a diameter of about 1.5 μm. The spot intensity is modulated by an electrooptic modulator fed by 8-bit (256 level) data.

If we use a 2D electrooptic modulator such as SLM and a near-field imaging system, we believe that the spot diameter can be reduced to a subwavelength scale and some 3D patterns can be directly fabricated with high resolution at a fast speed over a large area. We consider an upgraded laser writing system using 2D reconfigurable CGH on a phase-type SLM with a subwavelength optical imaging system, as shown in Fig. 16. The hologram patterns can be dynamically

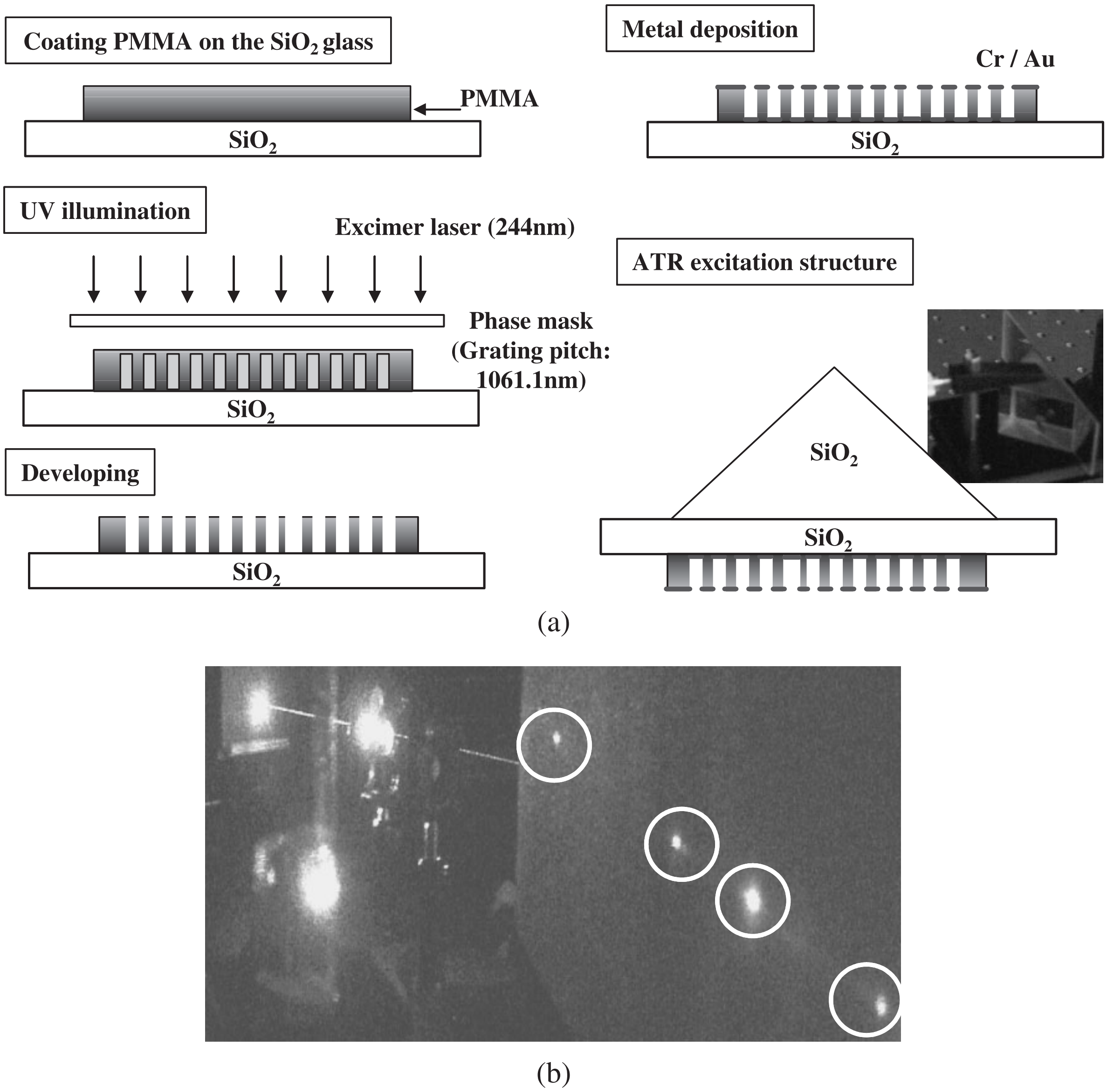

Fig. 17. (a) Fabrication process of the PMMA-based lamellar grating and (b) experimental result of the multifunctional lamellar grating under the illumination wavelength of 532 nm with the SPR excitation angle of 43.9°.

loaded so that they transfer arbitrary 2D beam patterns with the minimum focused spot size of ~250 nm and 2D gray-scale intensity profiles to the sample. The 2D reconfigurable dynamic CGH laser writing system can also control the gray-level intensity values of the reconstructing beam. The 2D dynamic CGH laser writing system would have the advantages of fast fabrication process, similar to a stepper in semiconductor lithographic system, good tolerance error performance because of its vibration-free characteristic and arbitrary 2D design feasibility of CGHs.

5.3 *Diffractive optic plasmonics devices*

As described in the above, the PMMA–metal grating SPR structures may have applications in some nanoscale photonics, biosensing or plasmonic integrated circuits. Figure 17(a) shows the fabrication process of the PMMA-based metal lamellar grating structure and experimental result of the multifunctional SPR excitation structure under the attenuated total reflection geometry. To form the PMMA–metal lamella grating structure, we inscribed the grating on the PMMA layer using a KrF excimer laser with the wavelength of 248 nm. After developing the PMMA, we deposited gold on the PMMA grating. From the experimental result shown in Fig. 17(b), we can see that the PMMA-based lamella metal grating can generate multiple diffracted beams and SPR excitation.

6. Concluding Remarks and Perspectives

The importance of diffractive optics will continue its rapid increase in the future. Diffractive optics will play important roles in realizing extraordinary optical functions, reducing the size of optical systems, and packaging and integration. Also, there will be more interests in dynamic optical elements for real-time optical information processing and display, which will require further investigation of improved or new optical materials such as liquid-crystal SLMs, photorefractive polymers, and holographic materials. Diffractive optics can be widely applied to bio-information technology, sub-wavelength-scale near-field optical imaging and plasmonics, nanofabrication, and high-capacity optical data storage systems. Also, much interest is focused on plasmonics, microfluidics, nanofabrication, and photonic integrated circuit applications in combination with diffractive optics technologies.

In this paper, we presented a unified approach to obtaining a thorough understanding and framework of the light field synthesis problem. We discussed the light field synthesis problems including 2D intensity distribution synthesis, 3D intensity distribution synthesis, and 3D image synthesis in terms of both the Fourier representation and the Hermite-Gaussian mode representation. The theoretical aspects of the field synthesis problem were focused on the mathematical formulation of the field synthesis problem, the objective functions and iterative optimization methods for minimizing and regularizing the objective functions.

Also, some DOE applications in, for example, IT (reconfigurable optical interconnection system and viewing-angle enhanced 3D display system), BT (dynamic holographic optical tweezing system and DOE-based plasmonic biochip structure), and NT (2D reconfigurable direct laser writing system and grating-based SPR excitation) were discussed. Diffractive optics has been widely studied for subwavelength-scale photonic circuits, fluorescence near-field microscopy, biosensing devices, and photonic display applications. Although diffractive optics has been studied quite intensively up to now, it still has many potential applications ranging from nanophotonic optical devices and circuits to near-field optical imaging and sensing, and is ripe for further active research.

1) G. M. Morris: Annu. Meet. Opt. Soc. Korea, 2003, p. 1.
2) *Encyclopedia Britannica* (Charles Schribner and Sons, New York, 1888) 9th ed., Vol. 24, p. 437.
3) J. Tarunen and F. Wyrowski: *Diffractive Optics for Industrial and Commercial Applications* (John Wiley & Sons, New York, 1997).
4) B. Kress and P. Meyrueis: *Digital Diffractive Optics: An Introduction to Planar Diffractive Optics and Related Technology* (John Wiley & Sons, New York, 2000).
5) V. A. Soifer: *Methods for Computer Design of Diffractive Optical Elements* (John Wiley & Sons, New York, 2001).
6) V. A. Soifer, V. V. Kotlyar and L. Doskolovich: *Iterative Methods for Diffractive Optical Elements Computation* (Taylor & Francis, London, 1997).
7) F. Wyrowski: J. Opt. Soc. Am. A **7** (1990) 961.
8) V. Kotlyar, P. G. Seraphimovich and V. A. Soifer: Opt. Lasers Eng. **29** (1998) 261.
9) H. Kim and B. Lee: Jpn. J. Appl. Phys. **43** (2004) L1530.
10) H. Kim and B. Lee: Opt. Lett. **30** (2005) 296.
11) E. G. Johnson and M. A. G. Abushagur: J. Opt. Soc. Am. A **12** (1995) 1152.
12) H. Aagedal, M. Schmid, T. Beth, S. Teiwes and F. Wyrowski: J. Mod. Opt. **43** (1996) 1409.
13) M. Johansson and J. Bengtsson: J. Mod. Opt. **47** (2000) 1385.
14) H. Kim, B. Yang and B. Lee: J. Opt. Soc. Am. A **21** (2004) 2353.
15) H. Kim and B. Lee: Jpn. J. Appl. Phys. **43** (2004) L702.
16) M. Kuittinen, P. Vahimma, M. Honkanen and J. Turunen: Appl. Opt. **36** (1997).
17) J. Rosen: Appl. Opt. **38** (1999) 6136.
18) Y. Sando, M. Itoh and T. Yatagai: Opt. Express **13** (2005) 1418.
19) R. Piestun and J. Shamir: Opt. Lett. **19** (1994) 771.
20) R. Piestun, B. Spektor and J. Shamir: J. Opt. Soc. Am. A **13** (1996) 1837.
21) R. Piestun and D. A. B. Miller: Opt. Lett. **26** (2001) 1373.
22) R. Piestun and J. Shamir: Proc. IEEE **90** (2002) 222.
23) U. Levy, D. Mendlovic, Z. Zalevsky, G. Shabtay and E. Marom: Appl. Opt. **38** (1999) 6732.
24) V. V. Kotlyar, S. N. Khonina and V. A. Soifer: J. Mod. Opt. **43** (1996) 1509.
25) G. Shabtay, Z. Zalevsky, U. Levy and D. Mendlovic: Opt. Lett. **25** (2000) 363.
26) J. Rosen and A. Yariv: Opt. Lett. **19** (1994) 843.
27) M. Born and E. Wolf: *Principles of Optics* (Cambridge University Press, New York, 1999) 7th ed.
28) J. Goodman: *Introduction to Fourier Optics* (McGraw-Hill, New York, 2004) 3rd ed.
29) H. Kim and B. Lee: Opt. Commun. **260** (2006) 383.
30) H. Kim, T. Kim, K. Choi, S. Han, I.-M. Lee and B. Lee: Proc. SPIE **5636** (2004) 431.
31) H. Kim and B. Lee: Opt. Eng. **43** (2004) 2671.
32) W. Singner and H. Tiziani: Appl. Opt. **37** (1998) 1249.
33) A. Rohrbach and W. Singer: J. Opt. Soc. Am. A **15** (1998) 2651.
34) W. Singer and K. Brenner: J. Opt. Soc. Am. A **12** (1995) 1913.
35) P. Lalanne: J. Opt. Soc. Am. A **14** (1997) 1592.
36) P. Lalanne and G. M. Morris: J. Opt. Soc. Am. A **13** (1996) 779.
37) L. Li: J. Opt. Soc. Am. A **13** (1996) 1870.
38) H. M. Ozaktas, Z. Zalevsky and M. A. Kutay: *The Fractional Fourier Transform with Applications in Optics and Signal Processing* (John Wiley & Sons, New York, 2001).
39) D. Dragoman: in *Progress in Optics*, ed. E. Wolf (Elsevier, Amsterdam, 1997) Vol. 37, p. 1.
40) M. J. Bastiaans: in *The Wigner Distribution-Theory and Applications in Signal Processing*, ed. W. Mecklenbrauker and F. Hlawatsch (Elsevier, Amsterdam, 1997) p. 375.
41) R. Piestun, Y. Y. Schechner and J. Shamir: J. Opt. Soc. Am. A **17** (2000) 294.
42) D. Abookasis and J. Rosen: J. Opt. Soc. Am. A **20** (2003) 1537.
43) Y. Sando, M. Itoh and T. Yatagai: Opt. Express **12** (2004) 2487.
44) Y. Sando, M. Itoh and T. Yatagai: Opt. Express **12** (2004) 6246.
45) C. Clinger, C. Cameron and M. Stanley: Computer **38** (2005) 46.
46) C. D. Cameron, D. A. Pain, M. Stanley and C. W. Slinger: Proc. SPIE **4109** (2000) 129.
47) D. J. Dallas: *The Computer in Optical Research* (Springer-Verlag, Berlin, 1980).
48) Y. Ichioka, M. Izumi and Y. Suzuki: Appl. Opt. **10** (1971) 403.
49) R. G. Dorsch, A. W. Lohmann and S. Sinzinger: Appl. Opt. **33** (1994) 869.
50) M. Lucente: Diffraction Specific Fringe Computation for Electro-Holography, Doctoral Thesis, MIT Dig. Electrical Engineering and Computer Science, Sept. 1994.
51) K. Choi, J. Kim, Y. Lim and B. Lee: Opt. Express **13** (2005) 10494.
52) K. Choi, H. Kim and B. Lee: Opt. Express **12** (2004) 5229.
53) K. Choi and B. Lee: Opt. Express **12** (2004) 2454.
54) M. A. Seldowitz, J. P. Allebach and D. W. Sweeney: Appl. Opt. **26** (1987) 2788.
55) S. Kirkpatric, C. D. Gelatt and M. P. Vecchi: Science **220** (1983) 671.
56) D. E. Goldberg: *Genetic Algorithms in Search Optimization and Machine Learning* (Addison-Wesley, Reading, MA, 1989).
57) R. W. Gerchberg and W. O. Saxton: Optik **35** (1972) 237.
58) J. R. Fienup: Appl. Opt. **21** (1982) 2758.
59) C. T. Kelly: *Iterative Methods for Optimization, Frontiers in Applied Mathematics* (Society for Industrial and Applied Mathematics, Philadelphia, 1999).
60) R. Liu, B. Gu, B. Dong and G. Yang: J. Opt. Soc. Am. A **15** (1998) 689.
61) M. G. Moharam and T. K. Gaylord: J. Opt. Soc. Am. **71** (1981) 811.
62) M. G. Moharam and T. K. Gaylord: J. Opt. Soc. Am. **72** (1982) 1385.
63) K. Knop: J. Opt. Soc. Am. **68** (1978) 1206.
64) R. Magnusson and T. K. Gaylord: J. Opt. Soc. Am. **69** (1979) 1777.
65) L. Li: J. Opt. Soc. Am. A **13** (1996) 1024.
66) A. Taflove and S. C. Hagness: *Computational Electrodynamics: The Finite-Difference Time-Domain Method* (Artech House, Boston, 2005) 3rd ed.
67) H. Raether: *Surface Plasmons on Smooth and Rough Surfaces and on Gratings* (Springer-Verlag, Berlin, 1988).
68) A. V. Zayats, I. I. Smolyaninov and A. A. Maradudin: Phys. Rep. **408** (2005) 131.

69) J. Homola, S. Yee and G. Gauglitz: Sens. Actuators B **54** (1999) 3.
70) B. Rothenhausler and W. Knoll: Nature **332** (1988) 615.
71) W. L. Barnes, A. Dereux and T. W. Ebbesen: Nature **424** (2003) 824.
72) P. Andrew and W. L. Barnes: Science **306** (2004) 1002.
73) S. Schultz, D. R. Smith, J. J. Mock and D. A. Schultz: Proc. Natl. Acad. Sci. U.S.A. **97** (2000) 996.
74) W. Zong, C. Thirstrup, M. H. Sørensen and H. C. Pedersen: Opt. Lett. **30** (2005) 1138.
75) J. E. Curtis, B. A. Koss and D. G. Grier: Opt. Commun. **207** (2002) 169.
76) H. Melville, G. F. Milne, G. C. Spalding, W. Sibbett, K. Dholakia and D. McGloin: Opt. Express **11** (2003) 3562.
77) T. Shiono and H. Ogawa: Appl. Opt. **33** (1994) 7350.
78) E. Pawlowski, H.-J. Dobschal, O. Falkenstörfer, W. Fürst, R. Steiner and R. Steigrüber: J. Mod. Opt. **47** (2000) 2437.
79) J. Schmidt, R. Voelkel, W. Stork, J. T. Sheridan, J. Schwider and N. Streibl: Opt. Lett. **17** (1992) 1240.
80) J. R. Leger, D. Chen and Z. Wang: Opt. Lett. **19** (1994) 108.
81) N. Streibl: J. Mod. Opt. **36** (1989) 1559.
82) J. H. Harris, R. K. Winn and D. G. Dalgoutte: Appl. Opt. **11** (1972) 2234.
83) S. Zhang and T. Tamir: IEEE J. Quantum Electron. **29** (1993) 2813.
84) S. Heinemann: Opt. Commun. **119** (1995) 613.
85) C. Heine and R. H. Morf: Appl. Opt. **34** (1995) 2476.
86) P. Blattner, H. P. Herzig, K. J. Weible, J. M. Teijido, H. J. Heimbeck and J. Rogers: J. Mod. Opt. **43** (1996) 1473.
87) K. Kostuk, Y.-T. Huang, D. Hetherington and M. Kato: Appl. Opt. **28** (1989) 4939.
88) B. R. Brown and A. W. Lohmann: Appl. Opt. **5** (1966) 967.
89) A. W. Lohmann and D. P. Paris: Appl. Opt. **7** (1968) 651.
90) J. P. Kirk and A. L. Jones: J. Opt. Soc. Am. **61** (1971) 1023.
91) J. N. Lee and A. Vanderlugt: Proc. IEEE **77** (1989) 1528.
92) T. H. Barnes, T. Eiju, K. Matsuda, H. Ichikawa, M. R. Taghizadeh and J. Turunen: Appl. Opt. **31** (1992) 5527.
93) P. Andres, V. Climent, J. Lancis, G. Minguez-Vega, E. Tajahuerce and A. W. Lohmann: Opt. Lett. **24** (1999) 1331.
94) J. Jahns and A. Huang: Appl. Opt. **28** (1989) 1602.
95) G. Minguez-Vega, M. Gruber, J. Jahns and J. Lancis: Appl. Opt. **44** (2005) 229.
96) J. Jahns, Y. H. Lee, C. A. Burrus, Jr. and J. L. Jewell: Appl. Opt. **31** (1992) 592.
97) Y. T. Huang, D. C. Su and Y. K. Tsai: Opt. Lett. **17** (1992) 1629.
98) R. Shechter, Y. Amitai and A. A. Friesem: Appl. Opt. **41** (2002) 1256.
99) S. Ahderom, M. Raisi, K. Lo, K. E. Alameh and R. Mavaddat: Proc. IEEE 5th Int. Conf. High-Speed Networks and Multimedia Communication, Korea, 2002, p. 239.
100) N. McArdle, M. Naruse, H. Toyoda, Y. Kobayashi and M. Ishikawa: Proc. IEEE **88** (2000) 829.
101) W. A. Crossland, I. G. Manolis, M. M. Redmond, K. L. Tan, T. D. Wilkinson, M. J. Holmes, T. R. Parker, H. H. Chu, J. Croucher, V. A. Handerek, S. T. Warr, B. Robertson, I. G. Bonas, R. Frankin, C. Stace, H. J. White, R. A. Wooley and G. Henshall: J. Lightwave Technol. **18** (2000) 1845.
102) A. Cassinelli, M. Naruse and M. Ishikawa: J. Lightwave Technol. **22** (2004) 315.
103) M. G. Taylor and J. E. Midwinter: J. Lightwave Technol. **9** (1991) 791.
104) J. E. Morris and M. R. Feldman: Appl. Opt. **33** (1994) 3683.
105) K. Choi and B. Lee: IEEE Photonics Technol. Lett. **17** (2005) 687.
106) J. Hahn, H. Kim, K. Choi and B. Lee: Appl. Opt. **45** (2006) 915.
107) P. Ehbets, H. Herzig, D. Prongue and M. Gale: Opt. Lett. **17** (1992) 908.
108) M. T. Gale, M. Rossi, J. Pedersen and H. Schutz: Opt. Eng. **33** (1995) 3556.
109) M. Gale, M. Rossi, H. Schutz, P. Ehbets, H. Herzig and D. Prongue: Appl. Opt. **32** (1993) 2526.